

J-PLUS: The Javalambre Photometric Local Universe Survey

A. J. Cenarro¹, M. Moles², D. Cristóbal-Hornillos¹, A. Marín-Franch¹, A. Ederoclite¹, J. Varela¹, C. López-Sanjuan¹, C. Hernández-Monteagudo¹, R. E. Angulo², H. Vázquez Ramió², K. Viironen¹, S. Bonoli¹, A. A. Orsi², G. Hurier², I. San Roman², N. Greisel², G. Vilella-Rojo², L. A. Díaz-García², R. Logroño-García², S. Gurung-López², D. Spinoso², D. Izquierdo-Villalba², J. A. L. Aguerri^{3,4}, C. Allende Prieto^{3,4}, C. Bonatto⁵, J. M. Carvano⁶, A. L. Chies-Santos⁵, S. Daflon⁶, R. A. Dupke^{6,7,8}, J. Falcón-Barroso^{3,4}, D. R. Gonçalves⁹, Y. Jiménez-Teja⁶, A. Molino¹⁰, V. M. Placco¹¹, E. Solano¹², D. D. Whitten¹¹, J. Abril², J. L. Antón², R. Bello², S. Bielsa de Toledo², J. Castillo-Ramírez², S. Chueca², T. Civera², M. C. Díaz-Martín², M. Domínguez-Martínez², J. Garzarán-Calderaro², J. Hernández-Fuertes², R. Iglesias-Marzoa², C. Iñiguez², J. M. Jiménez Ruiz², K. Kruuse², J. L. Lamadrid², N. Lasso-Cabrera², G. López-Alegre², A. López-Sainz², N. Maicas², A. Moreno-Signes², D. J. Muniesa², S. Rodríguez-Llano², F. Rueda-Teruel², S. Rueda-Teruel², I. Soriano-Laguía², V. Tilve², L. Valdivielso², A. Yanes-Díaz², J. S. Alcaniz^{6,13}, C. Mendes de Oliveira¹⁰, L. Sodré¹⁰, P. Coelho¹⁰, R. Lopes de Oliveira^{14,6,15,16}, A. Tamm¹⁷, H. S. Xavier¹⁰, L. R. Abramo¹⁸, S. Akras⁶, E. J. Alfaro¹⁹, A. Alvarez-Candal⁶, B. Ascaso²⁰, M. A. Beasley^{3,4}, T. C. Beers¹¹, M. Borges Fernandes⁶, G. R. Bruzual²¹, M. L. Buzzo¹⁰, J. M. Carrasco^{22,23}, J. Cepa^{3,4}, A. Cortesi¹⁰, M V Costa-Duarte¹⁰, M. De Prá⁶, G. Favole²⁴, A. Galarza⁶, L. Galbany²⁵, K. Garcia⁹, R. M. González Delgado¹⁹, J. I. González-Serrano²⁶, L. A. Gutiérrez-Soto⁹, J. A. Hernandez-Jimenez¹⁰, A. Kanaan²⁷, H. Kuncarayakti^{28,29}, R. C. G. Landim¹⁸, J. Laur¹⁷, J. Licandro^{3,4}, G. B. Lima Neto¹⁰, J. D. Lyman³⁰, J. Maíz Apellániz¹², J. Miralda-Escudé^{22,31}, D. Morate³, J. P. Nogueira-Cavalcante⁶, P. M. Novais¹⁰, M. Oncins^{22,23}, I. Oteo^{32,33}, R. A. Overzier⁶, C.B. Pereira⁶, A. Rebassa-Mansergas^{34,35}, R. R. R. Reis^{36,9}, F. Roig⁶, M. Sako³⁷, N. Salvador-Rusiñol^{3,4}, L. Sampedro¹⁰, P. Sánchez-Blázquez³⁸, W. A. Santos¹⁰, L. Schmidtobreick³⁹, B. B. Siffert⁴⁰, E. Telles⁶

(Affiliations can be found after the references)

September 10, 2021

ABSTRACT

The *Javalambre-Photometric Local Universe Survey* (J-PLUS) is an ongoing 12-band photometric optical survey, observing thousands of square degrees of the Northern hemisphere from the dedicated JAST/T80 telescope at the *Observatorio Astrofísico de Javalambre* (OAJ). T80Cam is a 2 deg² field-of-view camera mounted on this 83 cm-diameter telescope, and is equipped with a unique system of filters spanning the entire optical range (3 500–10 000 Å). This filter system is a combination of broad, medium and narrow-band filters, optimally designed to extract the rest-frame spectral features (the 3 700–4 000 Å Balmer break region, H δ , Ca H+K, the G-band, the Mgb and Ca triplets) that are key to both characterize stellar types and to deliver a low-resolution photo-spectrum for each pixel of the sky observed. With a typical depth of AB \sim 21.25 mag per band, this filter set thus allows for an indiscriminate and accurate characterization of the stellar population in our Galaxy, it provides an unprecedented 2D photo-spectral information for all resolved galaxies in the local universe, as well as accurate photo-z estimates (at the $\Delta z \sim 0.01$ –0.03 precision level) for moderately bright (up to $r \sim 20$ mag) extragalactic sources. While some narrow band filters are designed for the study of particular emission features ([OIII] λ 3727, H α / λ 6563) up to $z < 0.015$, they also provide well-defined windows for the analysis of other emission lines at higher redshifts. As a result, J-PLUS has the potential to contribute to a wide range of fields in Astrophysics, both in the nearby universe (Milky Way structure, globular clusters, 2D IFU-like studies, stellar populations of nearby and moderate redshift galaxies, clusters of galaxies) and at high redshifts (emission line galaxies at $z \approx 0.77, 2.2$ and 4.4, quasi stellar objects, etc). With this paper, we release ~ 36 deg² of J-PLUS data, containing about 1.5×10^5 stars and 10^5 galaxies at $r < 21$ mag. These numbers are expected to rise to about 35 million of stars and 24 million of galaxies by the end of the survey.

Key words. Surveys – Astronomical databases: miscellaneous – Techniques: photometric – Stars:general – Galaxy:general – Galaxies:general

1. Introduction

The success of large sky, broad band, photometric surveys like, e. g., the Sloan Digital Sky Survey (SDSS, York et al. 2000) demonstrated that multi-filter surveys can provide crucial information on the spectral energy distributions (SED) for millions of astronomical objects. This is particularly evident for some sci-

ence cases in which spectral resolution is not a limiting factor and, hence, multi-object spectroscopy is not critically required. One of the major advantages of photometric surveys relies on the fact that the object selection is not biased by any prior other than the limiting magnitude in each band, hence favoring complete-

ness and making possible the generation of more massive data sets.

In recent years, a growing number of multi-filter surveys with larger numbers of photometric bands like, e.g., COMBO-17 (Wolf et al. 2003), ALHAMBRA (Moles et al. 2008), COSMOS (Ilbert et al. 2009), MUSYC (Cardamone et al. 2010), CLASH (Postman et al. 2012), SHARDS (Pérez-González et al. 2013), have opened new ways to shed light on many areas in Astrophysics and Cosmology. These surveys share in common the use of a set of broad, intermediate and/or narrow band filters providing sufficient spectral information that enables addressing certain scientific cases without the need to resort to spectroscopy. The success of such surveys has motivated the design of new, challenging projects like, e.g., the Physics of the Accelerating Survey (PAU, Martí et al. 2014), the Javalambre-PAU Astrophysical Survey (J-PAS, Benitez et al. 2014a), and the Javalambre-Photometric Local Universe Survey, hereafter J-PLUS¹, whose presentation is the main goal of this paper.

As we explain next, the motivation for a survey like J-PLUS lies in the context of the J-PAS survey. J-PAS is a very wide field astrophysical survey to be developed at the Observatorio Astrofísico de Javalambre (OAJ; Cenarro et al. 2010, 2012, 2014). J-PAS will be conducted with the Javalambre Survey Telescope, JST/T250, a large-extended 2.5 m telescope, and JPCam, a panoramic 4.7 deg² camera with a mosaic of 14 large format CCDs, amounting to 1.2 Gpix. The main scientific driver of J-PAS is the measurement of radial Baryonic Acoustic Oscillations with an unprecedented accuracy. To achieve this, J-PAS is planned to observe around 8 500 deg² of the Northern Sky with a set of 54 contiguous, narrow band optical filters (145 Å width each, placed ~ 100 Å apart), plus two broad band filters at the blue and red sides of the optical range, and 3 SDSS-like filters. The filter set is designed to provide 0.3 % relative error ($0.003 \times [1 + z]$) photometric redshifts (photo-zs) for tens of millions of luminous red and emission line galaxies (ELGs), plus about two million quasi-stellar objects (QSOs) with similar photo-z quality, sampling an effective volume of ~14 Gpc³ up to $z = 1.3$. In addition, J-PAS is expected to detect hundreds of thousands of galaxy clusters and groups; produce one of the most powerful cosmological lensing surveys; and detect, classify and measure redshifts for thousands of SNe at the 1 % precision level (Xavier et al. 2014). All these observations should provide complementary constraints on Dark Energy, each of them suffering from different systematics, and thus providing a solid description of the nature of Dark Energy. Beyond these cosmological goals, the key to the J-PAS potential is its innovative approach. The use of the narrow band filters makes J-PAS to be equivalent to a low resolution Integral Field Unit (IFU) of the Northern Sky, providing the SED of every pixel of the sky and, ultimately, a 3D image of the Northern Sky with an obvious wealth of potential astrophysical applications².

The J-PLUS project is envisioned as a multi-filter survey aiming to support and complement J-PAS at both the technical and scientific levels. With a unique set of 12 broad, intermediate and narrow photometric bands in the optical range, J-PLUS was conceived to be implemented at the OAJ, using an 83 cm tele-

scope with a large field of view (FoV) and a very efficient, low read-out noise panoramic camera. Telescope, camera and filters are specifically designed under the main goal of conducting J-PLUS, hence optimizing the whole system to achieve the maximum outcome and efficiency of the survey.

J-PLUS' original goal to support the photometric calibration for J-PAS drove the definition of the J-PLUS filters. These filters have been conceived to retrieve accurate stellar SEDs and assign stellar templates to all the stars brighter than a certain magnitude. Those templates will ultimately allow to compute, for each star, synthetic magnitudes for the 59 J-PAS photometric bands in advance to J-PAS observations. With several dozens of stars in each of the 14 large format CCDs of JPCam it will be possible to compute the photometric zero points for each exposure of J-PAS (see, e.g., Varela et al. 2014). This calibration technique, together with alternative methods based on stellar locus in multiple J-PAS color-color diagrams, guarantees the success of the J-PAS calibration to uncertainties below 2 % in each filter.

In addition, the timing of J-PLUS is also an important asset. From the beginning, J-PLUS was thought to be conducted well in advance of J-PAS. First, because J-PLUS aims to observe most of the J-PAS footprint beforehand to support and complement the photometric calibration of J-PAS and its science. Second, because most of the technical developments related with the J-PLUS deployment (e.g., data reduction, pipelines, calibration procedures, scientific software, storage hardware, etc.) constitute the natural basis for J-PAS, in many cases requiring only minor modifications to be adapted to the J-PAS specifications.

The details of the photometric calibration of J-PAS using J-PLUS data will be addressed in a dedicated paper (Varela et al. in preparation). In this paper, however, we focus on the scientific value of J-PLUS. There are two main primary goals related with local Universe science that have been prioritized during the survey definition. The first one is the production of multi-filter photometric information for millions of Milky Way (hereafter MW) halo stars in the J-PAS footprint. This is a very valuable data set for multiple scientific cases in stellar astrophysics, like, e.g., the determination of atmospheric parameters, the detection of extremely metal poor stars, the study of brown dwarfs, variable sources, etc. The second primary goal is to optimally exploit the IFU-like science that J-PLUS can provide at very low spectral resolution. In particular, J-PLUS is aimed to focus on the detailed characterization of 2D stellar populations, star formation rates, and the role of environment for tens of thousands of galaxies in the local Universe ($z < 0.05$). In the context of these two main goals, the J-PLUS filter set has been defined to be particularly sensitive to rest-frame spectral features that are key to i) characterize the different stellar spectral types, luminosity classes and stellar metallicities, ii) disentangle ages and metallicities from the integrated light of local galaxies, and iii) determine reliable strengths of nebular emission lines such as H α and [OII] λ 3727.

The characteristics and strategy of the survey have been modulated to extract the maximum scientific return in many other areas of Astrophysics. J-PLUS will observe a significant fraction of the Northern sky in 12 photometric optical bands, hence providing multi-filter information for every pixel in the survey's footprint. This allows to address a very wide range of scientific cases, essentially all those that are benefited by i) the very large sky coverage of the survey; ii) the use of specific filters, some of them with narrow band passes located at key rest-frames spectral features; iii) a massive volume of data for most categories of astronomical objects, and iv) the time domain, as a result of the specific strategy to observe each field in the different

¹ <http://www.j-plus.es>

² One must bear in mind that, unlike in standard IFU spectroscopy, in the approach adopted by J-PLUS and J-PAS, data corresponding to different bands/spectral ranges may be acquired at different times. For this reason, the term “hyperspectral imaging” has also been proposed to dub the non-simultaneous, multi narrow, medium-width, and broad band photometry conducted by J-PLUS.

filters at different times plus the revisit of fields observed under poor atmospheric conditions.

Apart from describing the J-PLUS mission, the main goal of the present paper is to illustrate some of the most relevant scientific capabilities of J-PLUS based on real data. With this aim, in this paper we make public the first data release of the project, which amounts to $\sim 50 \text{ deg}^2$ of J-PLUS data split in two categories: $\sim 36 \text{ deg}^2$ in the J-PLUS footprint, constituting the so called J-PLUS Early Data Release, and $\sim 14 \text{ deg}^2$ in particularly interesting regions of the sky that were observed as part of the J-PLUS Science Verification Data. This data set is representative of the whole J-PLUS survey and allows to provide the reader with a flavor of the most relevant science cases that J-PLUS will address: MW science, stellar clusters, stellar populations of nearby and moderate redshift galaxies ($z < 0.015$), emission line studies, 2D IFU-like studies, high redshift galaxies, QSOs, clusters of galaxies, etc.

J-PLUS has already collected data over more than $1\,000 \text{ deg}^2$ of data, which should become publicly accessible during 2018. In the meantime, the *South-Photometric Local Universe Survey* (S-PLUS) is scanning the Southern sky from Cerro Tololo with identical telescope, camera and filter set as J-PLUS, thus strengthening the large scale character of both projects.

Overall, the paper is structured as follows. Section 2 introduces a general description of the survey making emphasis on the technical framework of J-PLUS: the OAJ, the JAST/T80 telescope and its panoramic camera T80Cam, the J-PLUS filter set, the survey strategy, the data reduction pipeline and, finally, the photometric calibration. Section 3 is devoted to describe the J-PLUS' Early Data Release and Science Verification data sets that are publicly released with this paper, on the basis of which Sect. 4 illustrates briefly some of the main science cases that will be covered by J-PLUS. Finally, the summary and conclusions are presented in Sect. 5.

2. J-PLUS definition and implementation

J-PLUS is a dedicated multi-filter survey of $\sim 8\,500 \text{ deg}^2$ that will be conducted from the OAJ during the next years using the JAST/T80 telescope. JAST/T80 is an 83 cm telescope with a large FoV, mounting T80Cam, a panoramic camera that provides a FoV of 2 deg^2 , and a set of 12 broad, medium and narrow-band filters. This filter set has been particularly defined to be sensitive to key stellar spectral features in the rest frame, thus being optimal for MW science and stellar population studies of galaxies in the local Universe. In addition, the survey strategy has been fine-tuned to optimize the scientific return in a wide range of applications in many other areas of Astrophysics.

In this section we describe the main technical characteristics of the survey, starting with the observatory (Sect. 2.1), telescope and camera (Sect. 2.2), and filters (Sect. 2.3), to continue with the survey strategy (Sect. 2.4), data reduction (Sect. 2.5), and calibration (Sect. 2.6).

2.1. The OAJ: an observatory for large sky surveys

The OAJ³ is an astronomical facility located at the Pico del Buitre of the Sierra de Javalambre, in Teruel, Spain. The site, at an altitude of 1957 m, has excellent astronomical characteristics in terms of median seeing (0.71 arcsec in V band, with a mode of 0.58 arcsec), fraction of clear nights (53 % totally clear, 74% with at least a 30% of the night clear) and darkness, with

Table 1. Main technical characteristics of the JAST/T80 telescope

Mount:	German equatorial
Optical configuration:	Ritchey Chrétien modified
M1 diameter:	83 cm
Field corrector:	3 spherical lenses
Effective collecting area:	0.44 m^2
Focus:	Cassegrain
F#:	4.5
Focal length:	3712 mm
Plate scale:	$55.56 \text{ arcsec mm}^{-1}$
FoV (diameter)	2.0 deg
Etendue:	$1.5 \text{ m}^2 \text{ deg}^2$
EE50 (diameter)	$9 \mu\text{m}$
EE80 (diameter)	$18 \mu\text{m}$

a typical sky surface brightness of $V \sim 22 \text{ mag arcsec}^{-1}$ at zenith during dark nights, a feature quite exceptional in continental Europe. Full details about the site testing of the OAJ can be found in Moles et al. (2010).

The OAJ was defined, designed and constructed to carry out large sky surveys with dedicated telescopes of unusually large FoVs. The two main telescopes at the OAJ are the Javalambre Survey Telescope (JST/T250), a 2.55 m telescope with 3 deg diameter FoV, and the Javalambre Auxiliary Survey Telescope (JAST/T80), an 83 cm telescope with a FoV diameter of 2 deg. JAST/T80 is the telescope dedicated to the development of J-PLUS, whereas J-PAS will be carried out at the JST/T250.

The definition, design, construction, exploitation and management of the observatory and the data produced at the OAJ are responsibility of the Centro de Estudios de Física del Cosmos de Aragón (CEFCA⁴). The OAJ project started in March 2010, mostly funded by the *Fondo de Inversiones de Teruel*, a programme supported by the local Government of Aragón and the Government of Spain, and is essentially completed since 2015. In October 2014, the OAJ was awarded with the recognition of Spanish ICTS (*Infraestructura Científico Técnica Singular*) by the Spanish Ministry of Economy and Competitiveness.

2.2. JAST/T80 and T80Cam

The JAST/T80 is an 83 cm telescope with a FoV of 2 deg diameter and fast optics (F#4.5), which drives a plate scale at the Cassegrain focal plane of $55.56 \text{ arcsec mm}^{-1}$. JAST/T80 has a German-equatorial mount. Figure 1 illustrates JAST/T80 inside the 6.2 m dome building at the OAJ. The optical tube assembly has also a very compact layout, with just 826 mm between M1 and M2. With an overall weight of around 2500 kg, JAST/T80 supports instruments at its Cassegrain focus of up to 80 kg.

The optical design of the JAST/T80 is based on a modified Ritchey-Chrétien configuration, including a field corrector of three spherical lenses of fused silica. The lens diameters are in the range 152–170 mm. The whole system is optimized to work in the optical range, from 330 to 1100 nm, yielding a polychromatic image quality better than $9.0 \mu\text{m}$ (EE50; diameter) inside the 13 cm diameter focal plane (3.1 deg^2), after having considered all error sources in the error budget. The design is also optimized to account for the J-PLUS filters and the T80Cam entrance window in the optical path. Table 1 illustrates a summary of the main technical characteristics of JAST/T80.

³ <http://www.oaj.cefca.es>

⁴ <http://www.cefca.es>



Fig. 1. View of the JAST/T80 telescope inside its dome at the Observatorio Astrofísico de Javalambre.

Because of the large FoV and fast optics, the JAST/T80 M2 is controlled actively with a hexapod that allows to perform small M2 corrections, keeping the system in focus and free of aberrations all over the FoV. This is done through a wave-front curvature sensing technique developed at CEFCA (see Chueca et al. 2012) that computes the optimal hexapod position for a given temperature and telescope pointing. This technique makes use of the scientific CCD of T80Cam, demanding only a few minutes every few hours of observation. In between such computations, M2 corrections are applied automatically in closed loop during the survey execution according to an empirically calibrated M2 control law. This control law is built on the basis of hundreds of telescope positions and temperatures. To improve the efficiency of the system, during the day time the JAST/T80 dome is air-conditioned at the expected temperature of the coming night to minimize temperature gradients in the telescope and camera.

Since the overall effective etendues of the OAJ systems are ultimately determined by the CCD filling factor at the telescope focal plane, the OAJ instrumentation is designed to take full advantage of the large FoV of the telescopes and the seeing conditions of the site. In this sense, JAST/T80 is equipped with an only instrument, T80Cam, a panoramic camera that will remain mounted at the telescope during the entire execution of J-PLUS, hence minimizing overheads in the operation due to instrument exchanges.

T80Cam includes a grade-1, back-side illuminated, low-noise $9.2 \text{ kpix} \times 9.2 \text{ kpix}$ CCD of $10 \mu\text{m pix}^{-1}$, specifically developed by Teledyne e2v (UK) for the J-PLUS and J-PAS projects. T80Cam provides a usable FoV of 2 deg^2 with a plate scale of $0.55 \text{ arcsec pix}^{-1}$. This full wafer CCD is read simultaneously from 16 ports, achieving read-out times of 12s with a typical read-out noise of $3.4 e^-$ (RMS). It has an image area of $92.16 \text{ mm} \times 92.32 \text{ mm}$ and a broadband anti-reflective coating for optimized performance in the range 380–850 nm.

T80Cam is a direct imaging camera designed to work in fast convergent beam at the Cassegrain focus of the JAST/T80, not having additional optical elements other than the J-PLUS filters and the cryostat entrance window, which is optically powered.

In fact, the camera entrance window is the fourth element of the JAST/T80 field corrector, that together with the filters has been accounted for when defining the optical design of JAST/T80. The window is a 10 mm thick, weakly powered field-flattener with an 8 mm distance between its inner surface and the focal plane.

T80Cam (Fig. 2; left) consists of two main subsystems, namely the filter and shutter unit (FSU) and the cryogenic camera. Apart from the mechanical flange to attach the instrument to the telescope, the FSU includes a two-curtain shutter provided by Bonn-Shutter UG (Germany) that allows taking integration times as short as 0.1 s with an illumination uniformity better than 1% over the whole FoV and the filter unit. The latter consists of two filter wheels with 7 positions each (Fig. 2; center), allowing to host all the 12 J-PLUS filters (6 filters plus an empty space in each filter wheel). This avoids the need to exchange filters during observations or from night to night, thus minimizing risks and maintenance downtimes. The camera system is a 1110S camera manufactured by Spectral Instruments (USA). Figure 2 (right) shows a view of T80Cam mounted on the Cassegrain focus of the JAST/T80. The cryogenic camera system consists of the cryostat, the powered entrance window, the science CCD, its control electronics, and the vacuum and cooling systems. The sensor is cryo-cooled to an operating temperature of -100°C with a cryo-tiger refrigeration system, a closed-cycle Joule-Thomson effect cryogenic refrigerator device. The chamber is evacuated to 10^{-4} Torr using a turbo dry vacuum pump.

A summary of the technical characteristics of T80Cam is presented in Table 2. In addition, full technical and managerial details on T80Cam can be found in Marin-Franch et al. (2012) and Marin-Franch et al. (2015).

2.3. J-PLUS filter set

The main goals of J-PLUS hinge on the accurate determination of SEDs of MW stars and nearby galaxies. It is therefore clear that the J-PLUS filter set must be sensitive to both the optical continuum and the most prominent spectral features. In this sense, it has been widely demonstrated that it is possible

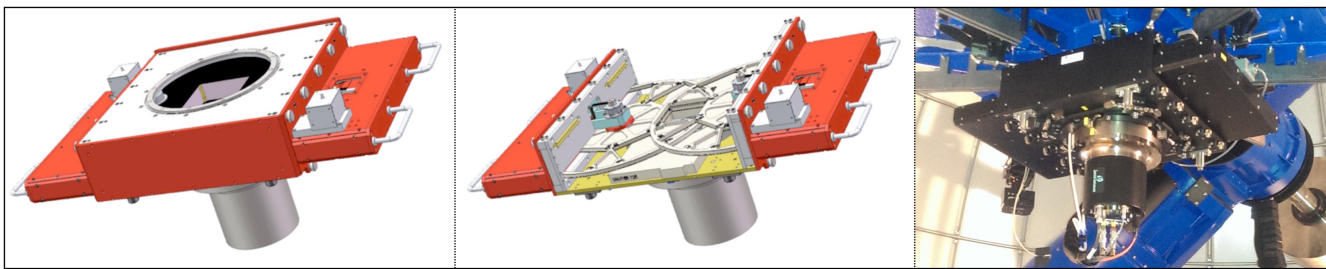


Fig. 2. *Left:* T80Cam 3D model design completely assembled. The top part of the instrument represents the filter and shutter unit, containing the shutter and the two filter wheels. The gray, cylindrical-shaped object underneath the filter and shutter unit represents the cryogenic camera. *Center:* the same view of T80Cam model after cover removal, showing the two filter wheels and the shutter. *Right:* T80Cam integrated at the Cassegrain focus of the JAST/T80 telescope.

Table 2. Main technical performances of the T80Cam panoramic camera at the JAST/T80 telescope

CCD format	9216×9232 pix
	$10 \mu\text{m pix}^{-1}$
Pixel scale	$0.55 \text{ arcsec pix}^{-1}$
FoV coverage	2.0 deg^2
Read out time	12 s
Read out noise	$3.4 \text{ e}^- \text{ pix}^{-1}$
Full well	$123\,000 \text{ e}^-$
CTE	0.99995
Dark current	$0.0008 \text{ e}^- \text{ pix}^{-1} \text{ s}^{-1}$
Number of filters	12

to retrieve reliable stellar SEDs with a set of around 10 to 15 intermediate-broad band optical filters centered at key spectral regions (e.g., Bailer-Jones 2004; Jordi et al. 2006; ?).

Following this strategy, the J-PLUS filter set consists of the 12 filters defined in Table 3. Among them, 4 are SDSS filters (g , r , i , and z ; Fukugita et al. 1996), providing the low frequency continuum, while 6 are intermediate band filters of 200–400 Å width, centred on key absorption features. These are the u filter, in common with J-PAS and located at the blue side of the 3 700–4 000 Å Balmer break region, and the filters $J0395$ for Ca H+K, $J0410$ for H δ , $J0430$ for the G-band, $J0515$ for the Mgb triplet, and $J0861$ for the Ca triplet. The J-PLUS filter set is completed with 2 narrow band filters, $J0378$ and $J0660$, also in common with the J-PAS filter set. These two filters are sensitive to the [OII]/ λ 3727 and H α / λ 6563 emission lines, respectively. The three filters in common with J-PAS are envisioned as an added value for the overall calibration procedure, as they will allow second order corrections of the zeropoints to anchor the J-PAS calibration.

The J-PLUS filters have been manufactured by SCHOTT (Switzerland). A detailed technical description of the filter requirements and design can be found in Marín-Franch et al. (2012). Fig. 3 shows the final efficiency curves of the filters.

The filter arrangement is tuned to provide scientifically valuable data for many fields of Astrophysics. Since the intermediate band filters are sensitive to the strengths of key features of old stellar populations, J-PLUS is very well suited for analyzing the stellar populations of nearby galaxies up to a limiting redshift of $z \sim 0.015$ (set by the typical filter width). In addition, the two narrow band filters are ideal for mapping the star formation rates in nearby galaxies in the range $0 < z < 0.05$. These considerations are fully addressed in Sect. 4.

Table 3. The J-PLUS filter system. Comments: (a) In common with J-PAS; (b) SDSS. Rest-frame key spectral features matching the location of narrow and mid band filters are also indicated.

Filter	Central		Comments
	Wavelength [Å]	FWHM [Å]	
u	3485	508	(a)
$J0378$	3785	168	[OII]; (a)
$J0395$	3950	100	Ca H+K
$J0410$	4100	200	H δ
$J0430$	4300	200	G-band
g	4803	1409	(b)
$J0515$	5150	200	Mgb Triplet
r	6254	1388	(b)
$J0660$	6600	138	H α ; (a)
i	7668	1535	(b)
$J0861$	8610	400	Ca Triplet
z	9114	1409	(b)

2.4. J-PLUS survey strategy

As explained in Sect. 1, one of the main goals of J-PLUS is to provide reliable stellar SEDs for millions of stars in the MW halo. For this goal, simulations reveal that it is sufficient reaching signal-to-ratio $\text{SNR} \geq 50$ for all stars brighter than $\sim 18 \text{ mag}^5$ in each J-PLUS filter. Given the T80Cam FoV of 2 deg^2 , there are more than one thousand stars per pointing and filter that reach $\sim 18 \text{ mag}$ in the Galactic halo. In terms of limiting magnitude, guaranteeing the above numbers is approximately equivalent to reaching $\sim 21.0 \text{ mag}$ for $\text{SNR} \geq 3$ for point-like sources, in a circular aperture of 3 arcsec. This depth suffices to guarantee unprecedented IFU-like science for thousands of nearby galaxies, both for 2D stellar populations gradients and SFR studies.

The exposure times of J-PLUS are set to reach the required signal-to-noise at $\sim 18 \text{ mag}$. Since J-PLUS fields are observed at different moon phases and moon distances, the optimal exposure time will depend on the brightness of the sky. For this reason, during commissioning we have empirically modelled the dependence of the sky brightness with respect to both distance and phase of the Moon. The estimated sky brightness at every J-PLUS pointing is then given as input to the exposure time calculator, which determines the particular exposure time for that pointing and time. Given the change in background, observing in the 12 filters takes typically about 35 minutes in dark time, and about 1.5 hours in bright time.

⁵ Unless explicated otherwise, magnitudes in this work will refer to the AB system.

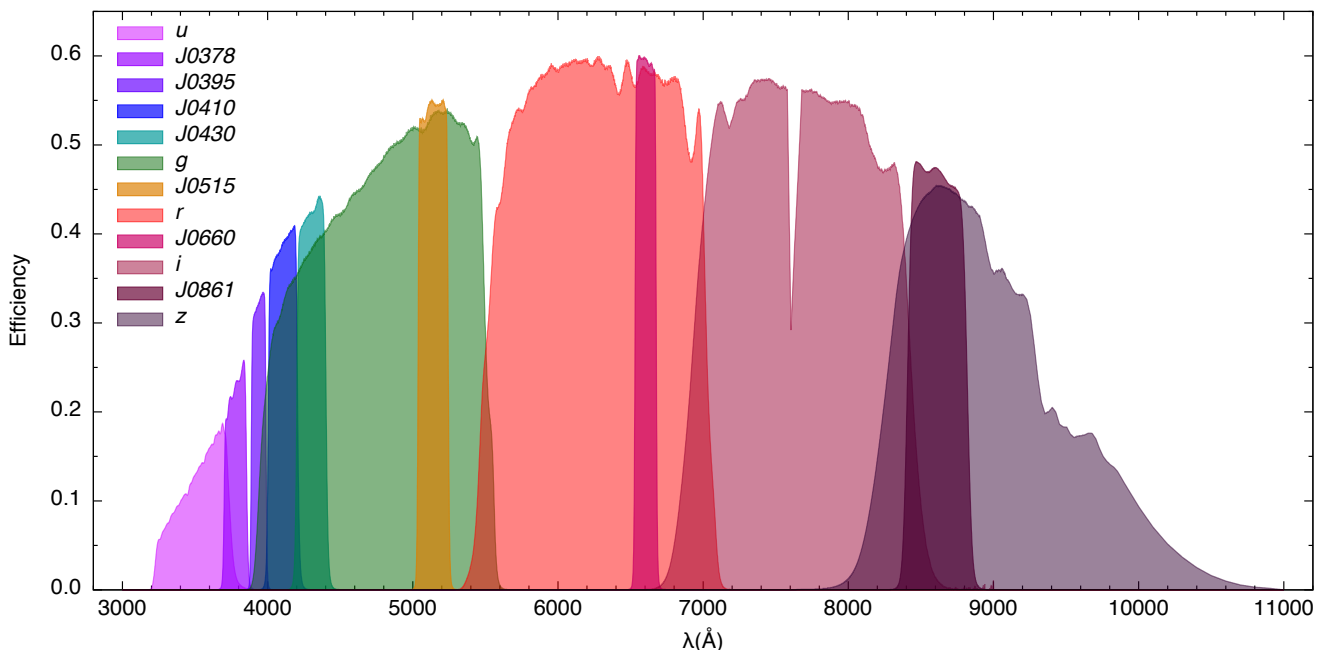


Fig. 3. Efficiency curves measured for the set of 12 J-PLUS filters, including the effect of the entire system (sky, mirrors, lenses, and CCD).

Table 4. Summary of the J-PLUS limiting magnitudes (for $\text{SNR} > 3$) and zero point calibrations. Two different quotes are given for the uncertainties in the zero point calibrations, one from EDR and another one from the amount of J-PLUS data collected until November 2017, after using the stellar locus and minimization in overlap areas in u , g , r , and i filters.

Filter	$m_{\text{lim}}^{\text{J-PLUS}}$	$m_{\text{lim}}^{\text{EDR}}$	$\langle \text{ZP} \rangle$	$\sigma_{\text{ZP}}^{\text{EDR}}$	$\sigma_{\text{ZP}}^{\text{J-PLUS}}$
u	21.00	21.6	21.13	0.037	0.023
J0378	21.00	21.5	20.54	0.084	0.026
J0395	21.00	21.4	20.32	0.072	0.026
J0410	21.25	21.5	21.30	0.058	0.018
J0430	21.25	21.5	21.37	0.050	0.018
g	22.00	22.2	23.58	0.042	0.013
J0515	21.25	21.4	21.52	0.039	0.012
r	22.00	21.9	23.52	0.039	0.010
J0660	21.25	21.3	21.04	0.042	0.012
i	21.75	20.8	23.25	0.042	0.012
J0861	20.50	20.8	21.54	0.052	0.017
z	20.75	20.5	22.63	0.024	0.017

With the goal of observing the same $\sim 8\,500\text{ deg}^2$ in the footprint of J-PAS, J-PLUS is scheduled in $\sim 4\,250$ pointings. For the most immediate observations, three priority areas have been selected amounting to about $1\,500\text{ deg}^2$:

- Priority Area – North 1 (PAN1): Defined by $120\text{ deg} < \text{RA} < 180\text{ deg}$ and $30\text{ deg} < \text{DEC} < 42\text{ deg}$, this area (580 deg^2) overlaps with eROSITA-Germany⁶ and UKIDSS-LAS-1⁷ fields.
- Priority Area – North 2 (PAN2): Defined by $180\text{ deg} < \text{RA} < 245\text{ deg}$ and $42.5\text{ deg} < \text{DEC} < 57\text{ deg}$, this area (610 deg^2)

overlaps with HETDEX⁸, ELAIS-N1, and ALHAMBRA-6⁹ fields.

- Priority Area – South (PAS): Defined by $0\text{ deg} < \text{RA} < 42.2\text{ deg}$ and $-5\text{ deg} < \text{DEC} < 8\text{ deg}$, this area (550 deg^2) overlaps with the SDSS Stripe 82¹⁰.

In general, each field is observed when its observability is optimal, typically within the requirements of airmass lower than 1.5 and seeing better than 1.5 arcsec. The ultimate observing sequence is managed by the J-PLUS Scheduler and Sequencer according to predefined observability, efficiency and image quality criteria.

2.5. J-PLUS pipelines and data management

The J-PLUS data are handled and processed using the data management software developed by the Data Processing and Archiving Unit (*Unidad de Procesado y Archivo de Datos*; hereafter UPAD) of CEFA. The technical details of J-PLUS data handling and data processing will be explained in a forthcoming article. Here we simply describe some of the steps involved in the treatment of the J-PLUS data presented in this paper.

During the execution of J-PAS and J-PLUS, the OAJ telescopes will produce thousands of images per night, amounting to several terabytes of data during a single, typical, observing night. To digest such a data rate, the pipelines have been designed to work automatically, i.e., with no human supervision. The OAJ hosts a set of dedicated servers that manage the transmission of the images from the camera servers to the OAJ storage and processing unit, where an online processing is done. This first processing uses a lightweight version of the pipeline, for real time visual inspection and first order diagnosis. Also, right after image acquisition, raw data are automatically transferred to the UPAD at CEFA for archival and a complete processing. This

⁶ <http://www.mpe.mpg.de/eROSITA>

⁷ <http://www.ukidss.org>

⁸ <http://hetdex.org>

⁹ <http://www.alhambraurvey.com>

¹⁰ <http://cas.sdss.org/stripe82/en/>

is done via a dedicated radio-link that connects the OAJ with CEFCA headquarters.

Once the raw data reach the main UPAD archive, they are automatically uploaded to a management database which stores all the metadata of the collected images. This database also stores all the processes done on the data, and is used to control whether the inputs for each stage are ready, and to automatically prepare the jobs to be executed. On a daily basis, the Data Management Software automatically processes the data collected during the last night in order to check their quality. It next updates the survey databases and feeds the Scheduler to compute the telescope targets of the following nights. Eventually, in order to optimize the scientific quality of the data, the pipelines reprocess all the images with the optimal master Calibration Frames (CFs) once they are available.

The image processing pipelines have three main stages. The first one is related to the generation of master CFs, which are used to correct for the instrumental imprint on the individual images at a later stage. These CFs consist of a master bias, the master dome or sky flats, a fringing pattern, and the illumination correction maps. To compute any of those CFs the pipeline requires as input the time interval and the instrumental configuration (telescope, camera and detector parameters, read-out configuration, etc). With this information in hand, the pipeline queries the database for the needed images and processes the master CFs. Once the CFs are generated, they are made available, through a web service, together with relevant information that allows to assess their quality. Finally, the master CFs require human validation to be used in further processing of science images.

The second stage is related to the processing of the different individual images. The pipeline corrects the instrumental signature using the validated CFs. The corrections (bias, flat fielding, fringing, etc.) that need to be applied to each image type are stored in the configuration files. Since the proper CFs for each image depend upon the required corrections, the observing epoch and the instrumental configuration, the pipeline must query the management database in order to assign the correct CFs. The pipeline also computes and assigns cold and hot pixel masks to every image, while generating masks for other contaminants (e.g., cosmic rays and satellite traces). If required, the pipeline can also interpolate the masked areas. For the detection and masking of cosmic ray hits, the pipeline uses an implementation of *L.A. Cosmic* (van Dokkum 2001). During the processing of the individual images, the pipeline calibrates the astrometry and the photometry (Bertin 2006), and generates a PSF map and a master PSF for each individual frame. Once the individual images are processed, a first catalogue is created over the individual images using *SExtractor* (Bertin & Arnouts 1996).

At a final stage, the pipeline combines the processed images from the same sky area to provide a deeper, photometric calibrated image for each filter. The pipeline makes use of the packages *Scamp* (Bertin 2006) and *Swarp* (Bertin et al. 2002) to perform the astrometric calibration and image coadding. The combined images for a given tile in the whole set of filters constitute a datacube. *SExtractor* source catalogues are extracted from the final tiles and datacubes and are stored in an internal database system. Two kind of catalogues are produced. In the first one, the source detection and segmentation are done independently for the combined images in each filter. In the second one, the detection and aperture definition is done in the *r* band, which is used as a reference image. Prior to computing the final catalogues, the PSF of each filter image is homogenized to match the one of the *r* filter, defined as reference filter in J-PLUS. This technique

was already used to produce the photometric catalogues for the ALHAMBRA survey (Molino et al. 2014).

The archival and processing of the J-PAS and J-PLUS data is done in a dedicated data center. The data center infrastructure and processing software are designed to handle the enormous data flow produced by the OAJ panoramic cameras, and specially to minimize the time required to transfer the images to the processing nodes, and to read/write data from/to disks. The main storage uses two different technologies. In order to feed data to the processing nodes, the data that are accessed frequently by the pipelines are kept in a disk storage cluster. The storage cluster runs a distributed file system providing access to the data through several servers, and together with the core network they provide an aggregated bandwidth above 50 Gbps to the processing servers. The permanent archive and the backup of the data is done in a robotic tape library. To process the J-PLUS images, the UPAD hosts dedicated nodes that have a large RAM to operate with the images without writing intermediate products to disk. The UPAD also counts with a large internal disk scratch used to store copies of the frequently required data, such as the CFs. More information on the facilities employed to process the J-PLUS data is provided in Cristóbal-Hornillos et al. (2014).

2.6. J-PLUS photometric calibration

The photometric calibration of J-PLUS faces two main challenges, namely the variety of observational conditions in which, throughout the project, J-PLUS images will be taken, and the use of a unique set of purposely defined filters. However, the difficulty of these tasks is to some extent alleviated by the large amount of external data made available by projects like SDSS (York et al. 2000), PanSTARRS (Kaiser et al. 2002) and Gaia (Gaia Collaboration et al. 2016).

In this context, with the ultimate goal of being able to calibrate J-PLUS at the widest variety of observing conditions, we choose to apply a battery of calibration procedures rather than relying on a single calibration technique. While the details of the calibration procedures will be presented in an upcoming work (Varela et al, in preparation), here we briefly outline the calibration procedures being currently applied on current J-PLUS data:

- *SDSS spectroscopy*. This is simply done by convolving the SDSS spectra with the spectral response for each filter of J-PLUS, yielding synthetic magnitudes whose comparison to the observed one provides estimates for the zero points (ZPs). Although the sky coverage of the SDSS spectra is smaller and sparser than J-PLUS photometry, it has the advantage that it can be used to calibrate those J-PLUS bandpasses that have no photometric counterpart. In particular, given the spectral coverage of SDSS spectra, these are used to calibrate the J-PLUS bandpasses from *J0395* to *J0861*, including *g*, *r* and *i*. With the installation of the BOSS spectrograph, the wavelength range of the spectra was extended to the blue, thus allowing the calibration of the *J0378* band in those areas of the sky with BOSS spectra available. However, *u* and *z* bands fall out always of the covered range by SDSS spectroscopy. Given the large FoV of T80Cam at JAST/T80 (2 deg²), it is not rare having dozens of high quality SDSS stellar spectra in a single J-PLUS pointing.
- *SDSS photometry*. The significant (~80%) overlap between J-PLUS and SDSS footprints allows to calibrate the J-PLUS broad band observations against the corresponding ones in SDSS, after applying the needed color term correc-

tions¹¹. This calibration technique is used to calibrate the u and z bands, uncovered by SDSS spectra.

- *Spectrophotometric standard stars*. The observation of spectrophotometric standard stars (hereafter SSSs) is the only procedure allowing to calibrate the full J-PLUS bandpass system, as long as the SSS spectra cover the full spectral range of the J-PLUS filter system. The main sources for the SSSs are the spectral libraries CALSPEC¹², the Next Generation Spectral Library¹³ and STELIB (Le Borgne et al. 2003). Following the classical calibration procedure, each SSS is observed at different airmasses along the night to derive the extinction coefficient and the photometric ZP of the system. As it is well known, for this procedure to be accurate the atmospheric conditions must be very stable. The SSS technique is critical in the calibration of the $J0378$ filter, since neither SDSS photometry nor SDSS spectroscopy cover this bandpass.

The current procedures are thought to be applied to any single exposure or any combination of exposures in a given filter, independently of the observations in any other band. However, by combining the information from different bands, it should also be possible to apply methods that enable to anchor the calibration across the spectral range. One particularly promising approach is the use of the stellar locus (Covey et al. 2007; High et al. 2009; Kelly et al. 2014), which optimally suits in systems with large FoVs as those at the OAJ. This procedure profits from the way stars with different stellar parameters populate colour-colour diagrams, defining a well limited region (stellar locus) whose shape depends on the specific colors used. A specific stellar locus approach for the calibration of J-PLUS has been developed, obtaining consistent zero point calibrations over the full J-PLUS spectral range with $\sigma_{ZP} \lesssim 0.02$. The details of this procedure and its application to J-PLUS data will be presented in a future work.

In Table 4 we summarise the median zero points (ZPs) for each J-PLUS filter in the EDR. We also present the typical uncertainty in the calibration, ranging from $\sigma_{ZP} \sim 0.06$ at the bluer bands to ~ 0.04 at the redder ones. These uncertainties were estimated from the comparison of duplicated sources in the J-PLUS overlapping areas, and should be accounted for in the photometry error budget of all sources. We also include the preliminary ZPs obtained through the use of stellar locus on the entire amount of J-PLUS data collected until November 2017 (rightmost column). A significant improvement in the ZP uncertainties is found in the latter case.

3. J-PLUS Early Data Release (EDR)

With the final J-PLUS strategy and depths frozen, we have identified and curated a subset of J-PLUS tiles that are representative of the J-PLUS project in terms of depth, PSF, photometric calibration accuracy, etc. These tiles compose the J-PLUS EDR and are publicly available at the J-PLUS web portal¹⁴.

¹¹ Due to differences in the effective transmission curves between SDSS and J-PLUS photometric systems, it is needed to apply color term corrections to the SDSS photometry to obtain the corresponding J-PLUS photometry. These corrections are of particular importance in the case of the u band where filters are known to be significantly different.

¹² <http://www.stsci.edu/hst/observatory/crds/calspec.html>

¹³ <https://archive.stsci.edu/prepds/stisngs1/>

¹⁴ https://www.j-plus.es/datareleases/early_data_release

The J-PLUS EDR comprises 18 J-PLUS pointings amounting to 31.7 deg^2 after masking. The tiles belonging to the J-PLUS EDR were selected to i) have a limiting magnitude as close as possible to the final J-PLUS goal in all the filters simultaneously, ii) have no evident issues neither in the photometry nor in the source catalogues, and iii) define a reasonably compact region on the sky, as presented in Fig. 4.

The FWHM and ellipticity distributions of the J-PLUS EDR tiles in the r band are shown in Fig. 5. These values are consistent with those of the parent J-PLUS data, and show average FWHM lower than 1.5 arcsec. The completeness for stars (point-like sources) and galaxies (extended sources) was computed by comparing with the SDSS dataset in the common areas (see López-Sanjuan et al. 2018, for details). The median 50 % completeness in J-PLUS EDR is reached at $r = 21.5$ for stars and $r = 21.0$ for galaxies. For reference, the median 90 % completeness is reached at $r = 21.3$ for stars and $r = 20.5$ for galaxies.

The EDR limiting magnitude distribution in the 12 J-PLUS bands is presented in Table 4 and in Fig. 6, where we indicate the target J-PLUS limits by means of a vertical dotted line. We can appreciate that, with the exception of the i band, the EDR is fairly close to the targeted J-PLUS magnitudes. Additionally, as expected, the data is very homogeneous by construction, exhibiting variations in depth of ~ 0.1 magnitudes.

The EDR sources have been morphologically classified into stars or galaxies using a Bayesian approach (see, for further details, López-Sanjuan et al. 2018). In this work we find that J-PLUS sources exhibit two distinct populations in the magnitude vs. concentration plane, corresponding to compact (stars) and extended (galaxies) sources. We model the two-population distribution and used a number density prior based on EDR data to estimate the Bayesian probability of each source to be either a star or a galaxy. This procedure is applied in each pointing separately in order to account for varying observing conditions and the particular MW stellar density in that field. Finally, we combine the morphological information from g , r , and i broad bands in an attempt to improve the classification of low signal-to-noise sources. The derived probabilities are used to compute the pointing-by-pointing number counts of stars and galaxies (López-Sanjuan et al. 2018). The former increases as we approach to the Milky Way disk, and the latter are similar across the probed area. The comparison with SDSS in the common regions is satisfactory up to $r \sim 21$, with consistent number counts of stars and galaxies, and consistent distributions in concentration and $(g - i)$ colour spaces.

To summarise, the J-PLUS EDR tiles are representative of the parent J-PLUS data in terms of PSF and photometric quality, and they display depths similar to the J-PLUS data gathered so far. As a representative pointing, the color composite of the J-PLUS EDR tile 4951 is presented in Fig. 7. Likewise, Fig. 8 provides the nearby galaxy NGC4470 as seen in the 12 J-PLUS bands.

3.1. J-PLUS Science Verification Data (SVD)

In addition to the J-PLUS EDR presented in the previous section, several tiles belonging to the J-PLUS science verification data (hereafter SVD) are also released with the present paper. These data were acquired before the beginning of J-PLUS, targeting particularly well-known objects to test and challenge the science capabilities of J-PLUS. The J-PLUS SVD pointings released with this paper¹⁵ are:

¹⁵ <https://www.j-plus.es/datareleases/svd>

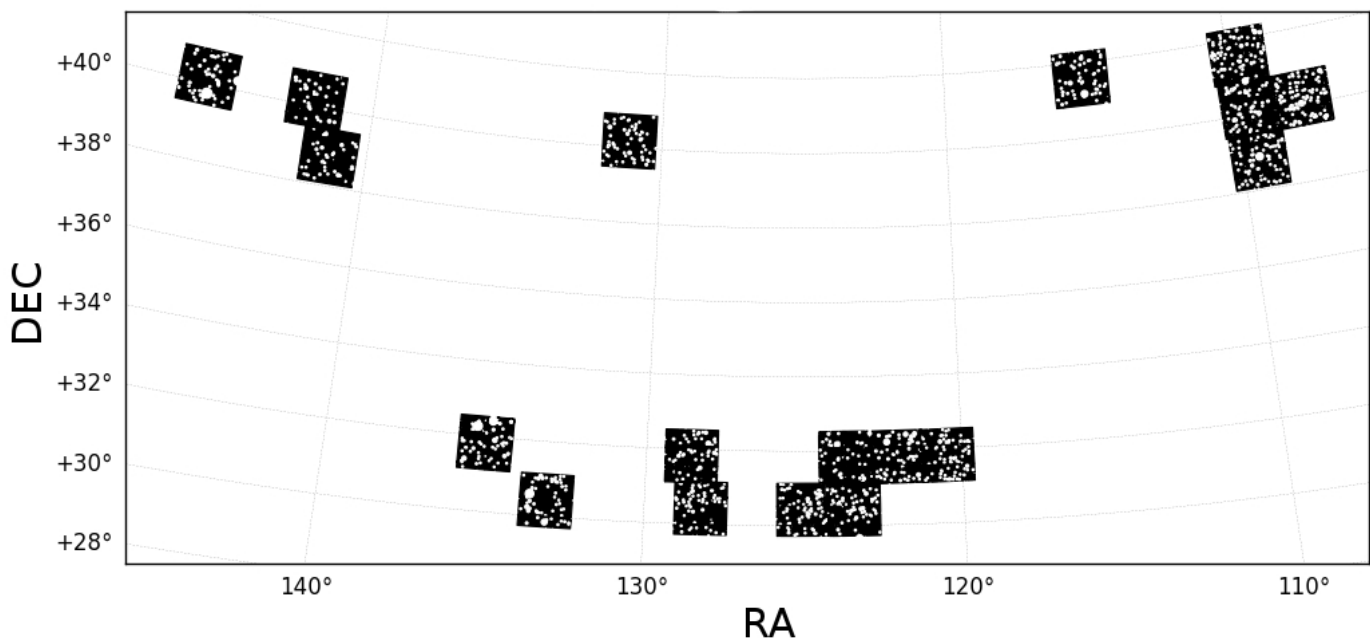


Fig. 4. Footprint of the J-PLUS EDR. It covers 31.7 deg^2 after masking low exposure regions, the surroundings of bright stars, observational reflections/artifacts, and overlapping areas.

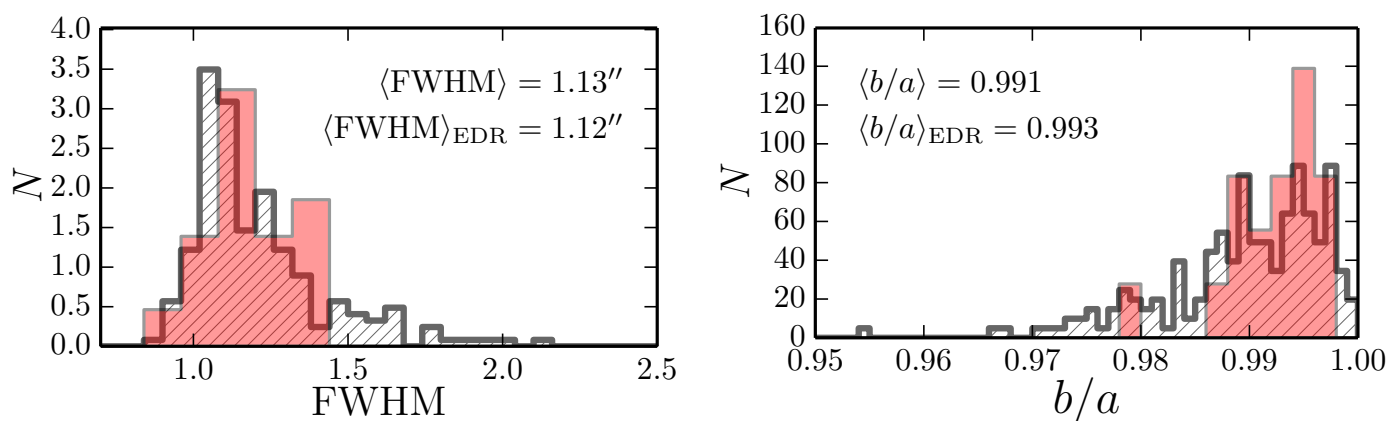


Fig. 5. FWHM and ellipticity (b/a ratio) statistics of the J-PLUS EDR (red histograms) and the whole J-PLUS data gathered so far (gray hatched histograms) as measured in r band on objects classified as stars. Histograms are normalised and thus represent probability.

- 1 pointing centered at the MW globular cluster M15 (Bonatto et al. 2018).
- 3 pointings covering continuously the galaxy clusters A2589 ($z = 0.0414$) and A2593 ($z = 0.0440$). The analysis of these data is presented in Molino et al. (2018).
- 3 pointings for the galaxies M101, M49 and the Arp313 triplet of galaxies. The nearby galaxies in these pointings, including NGC4470 ($z = 0.0079$, Fig. 8), are studied in Logroño-García et al. (2018) and San Roman et al. (2018b).
- 1 pointing centered at the Coma cluster of galaxies.
- 6 pointings targeting several Milky Way planetary nebulae.

We stress that the J-PLUS SVD are not strictly considered J-PLUS data due to the following reasons: i) the photometric depths and observing conditions could be slightly different to the ones set for J-PLUS; ii) the observed fields can be either outside the J-PLUS footprint or have different coordinates than the predefined J-PLUS tiles; iii) a versioning of the SVD is not performed, i.e., the data of the different projects could have been

processed with different versions of the pipeline; iv) the source catalogs are not necessarily the official catalogs created by the UPAD inside the J-PLUS collaboration, but could have been produced by different J-PLUS members; and v) the database backend is neither available nor designed for these data.

Still, the J-PLUS SVD provides very interesting data that deserve to be presented and made public to illustrate some science cases that can be developed with J-PLUS. Overall, the combination of J-PLUS EDR and SVD provides a total amount of 32 JAST/T80Cam pointings observed with the 12 J-PLUS filters, covering an area of $\sim 64 \text{ deg}^2$ before masking corrections. On the basis of these data, in the following section we focus on some of the most relevant J-PLUS science cases.

4. J-PLUS Science Cases

The J-PLUS coverage of the optical SED with 12 photometric bands permits a great variety of studies, including MW stars

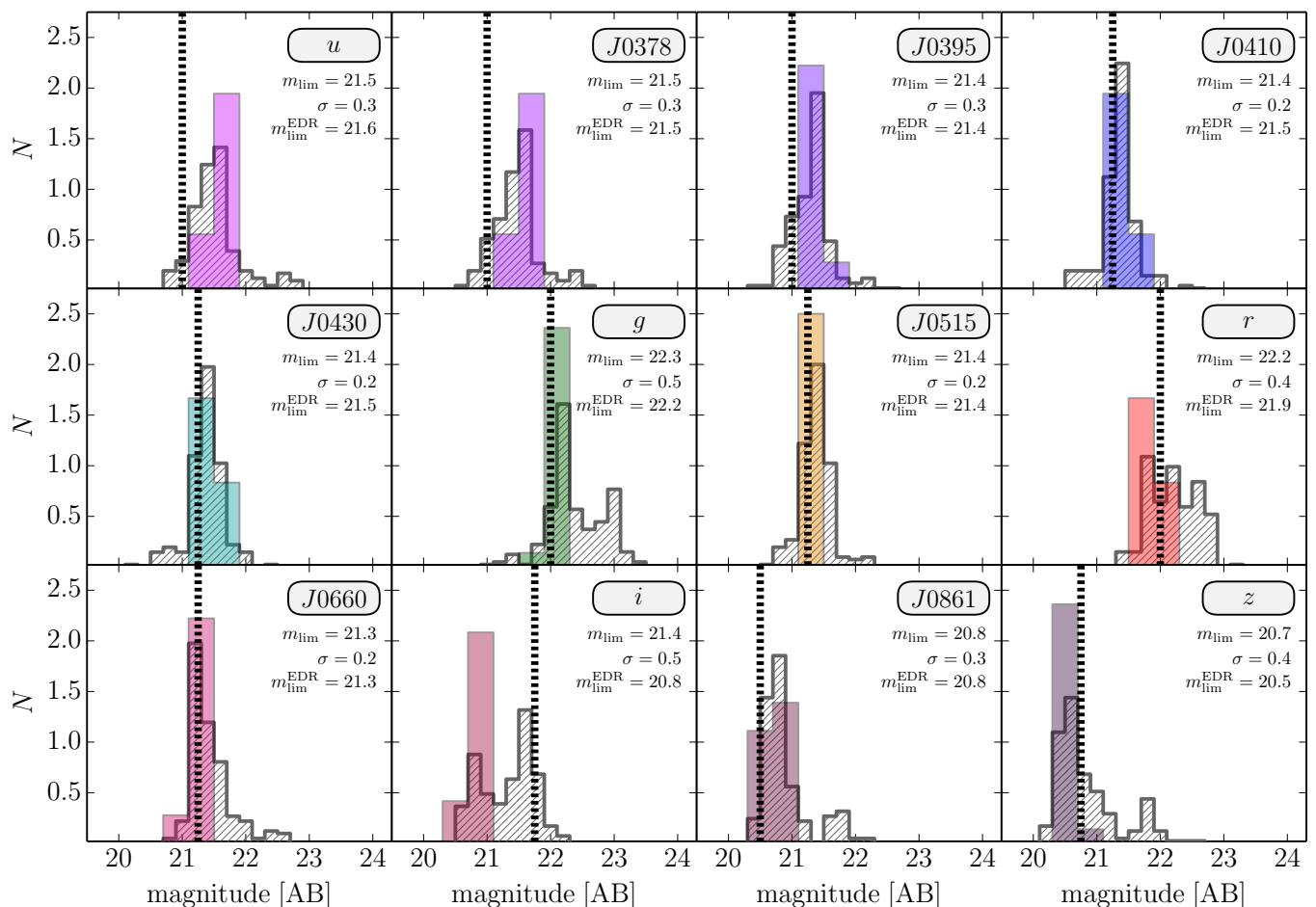


Fig. 6. Normalised distribution of the limiting magnitudes (3σ , $3''$ aperture) of the J-PLUS EDR tiles (18 tiles, coloured solid histograms) and the whole J-PLUS data gathered so far (205 tiles, gray hatched histograms). The black vertical lines mark the targeted J-PLUS limiting magnitudes as reported in Table 4. The legend in the panels provide the median of the limiting magnitudes in the two data samples.

(Sect. 4.1), both nearby and much more distant galaxies at specific redshift windows (Sects. 4.2, 4.3), and variable objects (Sect. 4.4). In the next subsections we present representative examples of some of those topics, demonstrating the capabilities and the potential of J-PLUS.

4.1. Exploring the MW halo

In the next years, the Gaia mission is going to provide the most detailed view ever made of the 3D-structure of the MW, improving our knowledge on its composition, formation, and evolution. Because of its survey strategy and performance, J-PLUS can help to complement Gaia’s science on the MW halo. For instance, J-PLUS expands the Gaia wavelength coverage to both the near-IR and the UV. This extension in the UV range is of particular interest since the Gaia spectrophotometric system is not very efficient below 400 nm. In this sense, the bluest J-PLUS filters can help to disentangle the determinations of extinction (A_V) and effective temperature (T_{eff}) by Gaia at fainter magnitudes and at the low metallicity regime. In addition, since there exists a time baseline of more than 20 years between the Tycho-2 and SDSS catalogues on one side, and J-PLUS on another, and the J-PLUS astrometry will be anchored on that of

Gaia, J-PLUS can extend the proper motion determinations by Gaia down to a fainter limit of $g \sim 22$ mag.

In general terms, the halo of the MW provides a unique laboratory to explore the nature of galaxy assembly in exquisite detail, the relation between the globular clusters and field star populations, the formation and evolution of the first generations of stars, and the nucleosynthesis in the early Universe, to name a few topics. Below we summarize a few examples showing the potential of J-PLUS on these fronts.

4.1.1. Stellar parameters of MW stars

With the advent of narrow-band photometric surveys such as J-PLUS it is possible to provide a method to obtain the photometric stellar parameter estimates required by the next generation of stellar population studies. The narrow- and intermediate-band filters implemented by J-PLUS are centred on key stellar absorption features, which are sensitive to stellar parameters and chemical abundances, including effective temperature (T_{eff}), surface gravity ($\log g$), metallicity ($[\text{Fe}/\text{H}]$), as well as carbon abundance ($[\text{C}/\text{Fe}]$) and magnesium abundance ($[\text{Mg}/\text{Fe}]$). Examples include the Ca II H & K lines, the CH G -band molecular feature close to $H\delta$, and the Mg triplet, associated with the

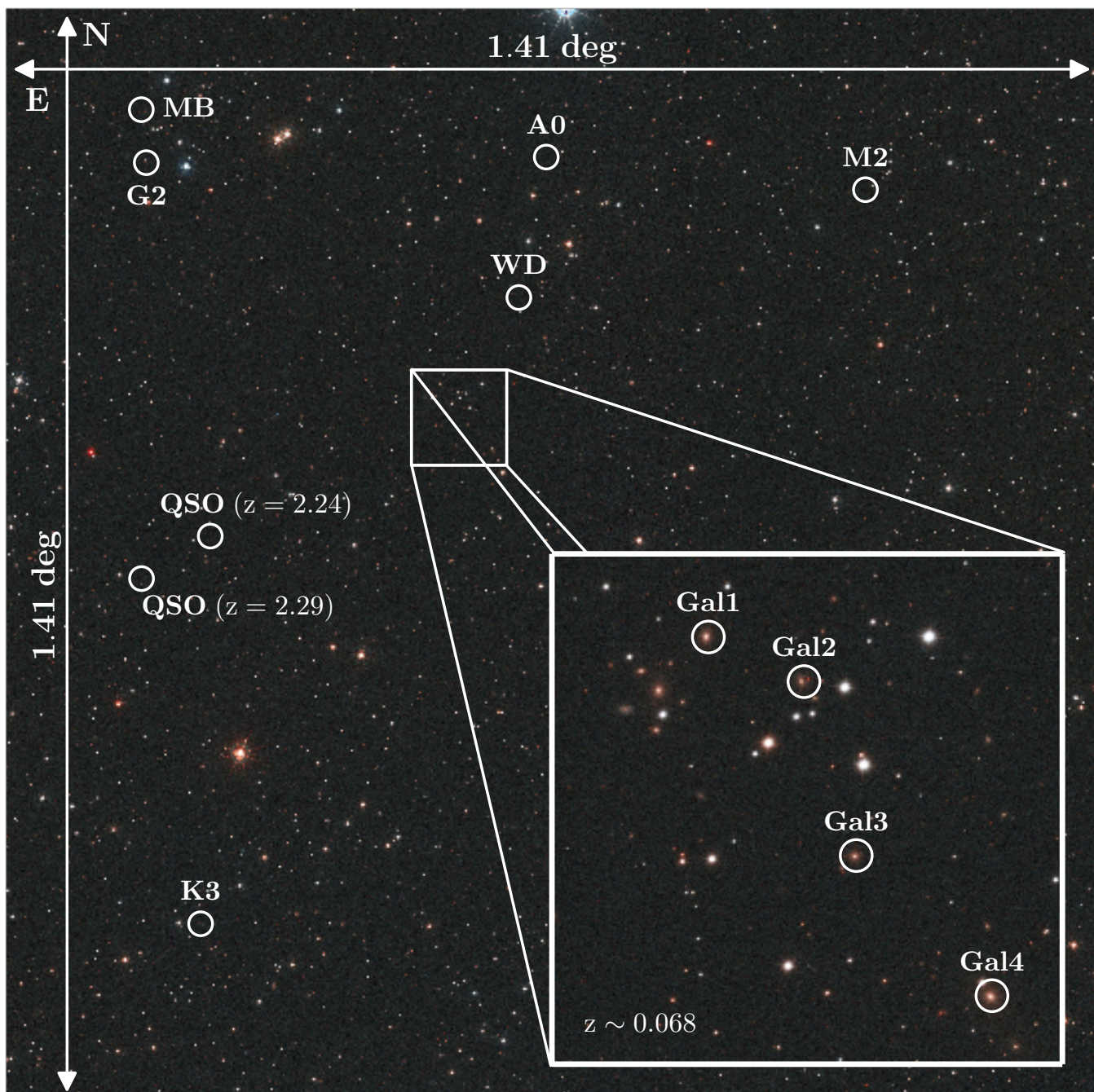


Fig. 7. Color composite of the J-PLUS EDR tile 4951. Several astrophysical objects analysed in the present paper are labelled in the figure: four MW stars of different spectral types (A0, G2, K3, M2); one white dwarf (WD), a minor body (MB) of the Solar System, four galaxies belonging to a $z = 0.068$ nearby cluster (Gal1, Gal2, Gal3, Gal4), and two high- z quasars (QSOs).

$J0395$, $J0430$, and $J0515$ filters, respectively. An illustration of the SEDs of different stellar spectral types as seen by J-PLUS is presented in Fig. 9.

While the J-PLUS filters are optimally placed along the SED to enable detection of key absorption features, mapping their behaviour to overall estimates of temperature, metallicity, and the elemental abundances of C and Mg presents a highly degenerate problem. For example, at higher temperatures, ($T_{\text{eff}} \gtrsim 6000$ K), the CH molecule dissociates while the $H\delta$ line broadens to the extent of disrupting the carbon feature. The Ca II K line provides

an ideal indicator for stellar metallicity, but also exhibits a temperature dependence that prevents the direct use of line widths to estimate metallicity.

Multiply-degenerate parameter spaces such as this can be approached through the application of machine learning algorithms. Recently, a subset of machine learning known as Artificial Neural Networks (ANNs) have shown great promise as robust tools for stellar spectral classification (Kheirdastan & Bazarghan 2016). We have made use of these pattern

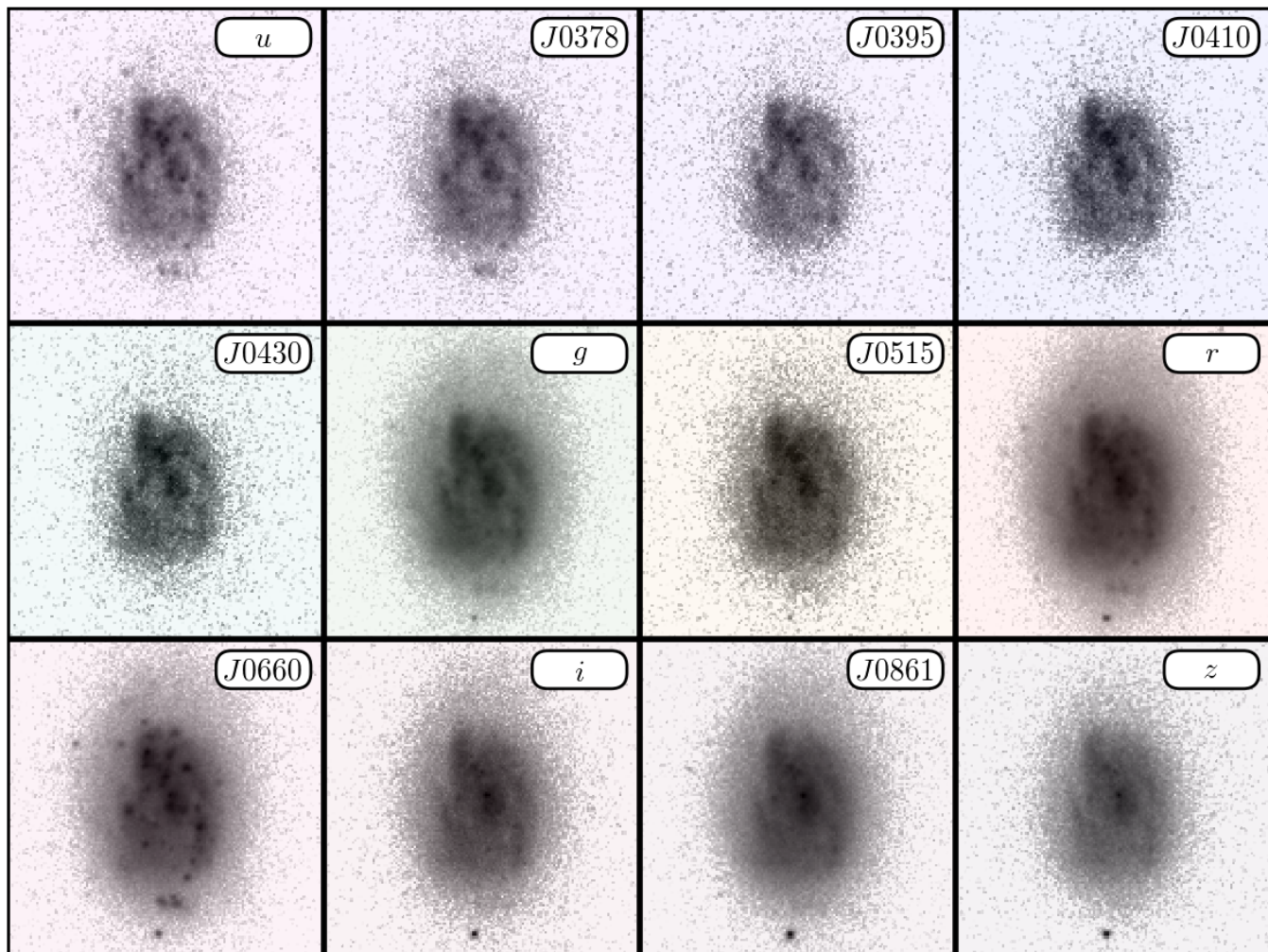


Fig. 8. NGC4470 in the 12 J-PLUS bands. This nearby galaxy is ideal to illustrate how a typical HII galaxy is seen by J-PLUS, with plenty of young star-forming knots highlighted on the bluest filters (u and $J0378$; covering [O II] emission line) and $J0660$ (covering $H\alpha$ and [N II] emission lines). As expected, these knots are essentially absent in the reddest bands, which rather trace the underlying old stellar population of the galaxy.

recognition tools for stellar parameter determination using the J-PLUS photometric system.

The training dataset for the ANNs is taken from the SEGUE (Yanny et al. 2009) database, in which stellar parameters were derived from the observed (flux calibrated) spectra using the SEGUE Stellar Parameter Pipeline (SSPP, Lee et al. 2008). Synthetic magnitudes are first generated for these spectra by convolution with J-PLUS filter response functions. Upon verification of the proper network inputs, functional forms for these synthetic magnitudes are then calibrated to the J-PLUS photometric system using ~ 1000 overlapping observations from the J-PLUS EDR.

After training and for the final validation of the ANN methodology, the temperature and metallicity networks are next applied to J-PLUS photometry using the EDR. Figure 10 depicts the one-to-one fit and residual plot for the network prediction against accepted SSPP estimate. The effective stellar temperature is recovered with a dispersion of $\sigma_{T_{\text{eff}}} = 158$ K, while the expectations for the metallicity is $\sigma_{[\text{Fe}/\text{H}]} = 0.31$ dex. We note deviations in the low temperature regime of the network estimates ($T_{\text{eff}} < 4750$ K). We attribute this underestimation to edge effects inherent in network estimates approaching the interpolation range of the training set in addition to an increasing uncertainty

in the temperature estimates made by the SSPP in this range. An increase in scatter can be seen near $T_{\text{eff}} = 6500$ K, where we expect a presence of variable stars whose spectroscopic and photometric temperature were estimates determined at different phases in the stellar pulsation.

J-PLUS photometry also exhibits a crucial sensitivity to changes in the surface gravity of stellar atmospheres. In particular, gravity sensitive regions around the Balmer break (3700~4000 Å), as well as the Paschen break, CaII triplet lines and TiO bands (e.g., Cenarro et al. 2001a, 2009), present in the $J0378$ and $J0861$ filters, respectively, can be used. Pressure broadening affects the continuum in these regions, corresponding to a detectable difference in flux between low and high gravity environments (Vickers et al. 2012). This behaviour is shown in Fig. 11, where the gravity sensitive color $(J0378-J0410)_0$ is shown against the temperature dependent color $(J0515-J0861)_0$, and where the 0 subscripts denotes “reddening corrected”.

An approach alternative to ANNs is a direct search for optimal atmospheric parameters via an interpolation in a model library, obtained from Kurucz model atmospheres, as described in Allende Prieto (2016); Allende Prieto & Nahar (2018). Our analysis is based upon the FERRE code (Allende Prieto et al. 2006, and subsequent updates). The optimization algorithm

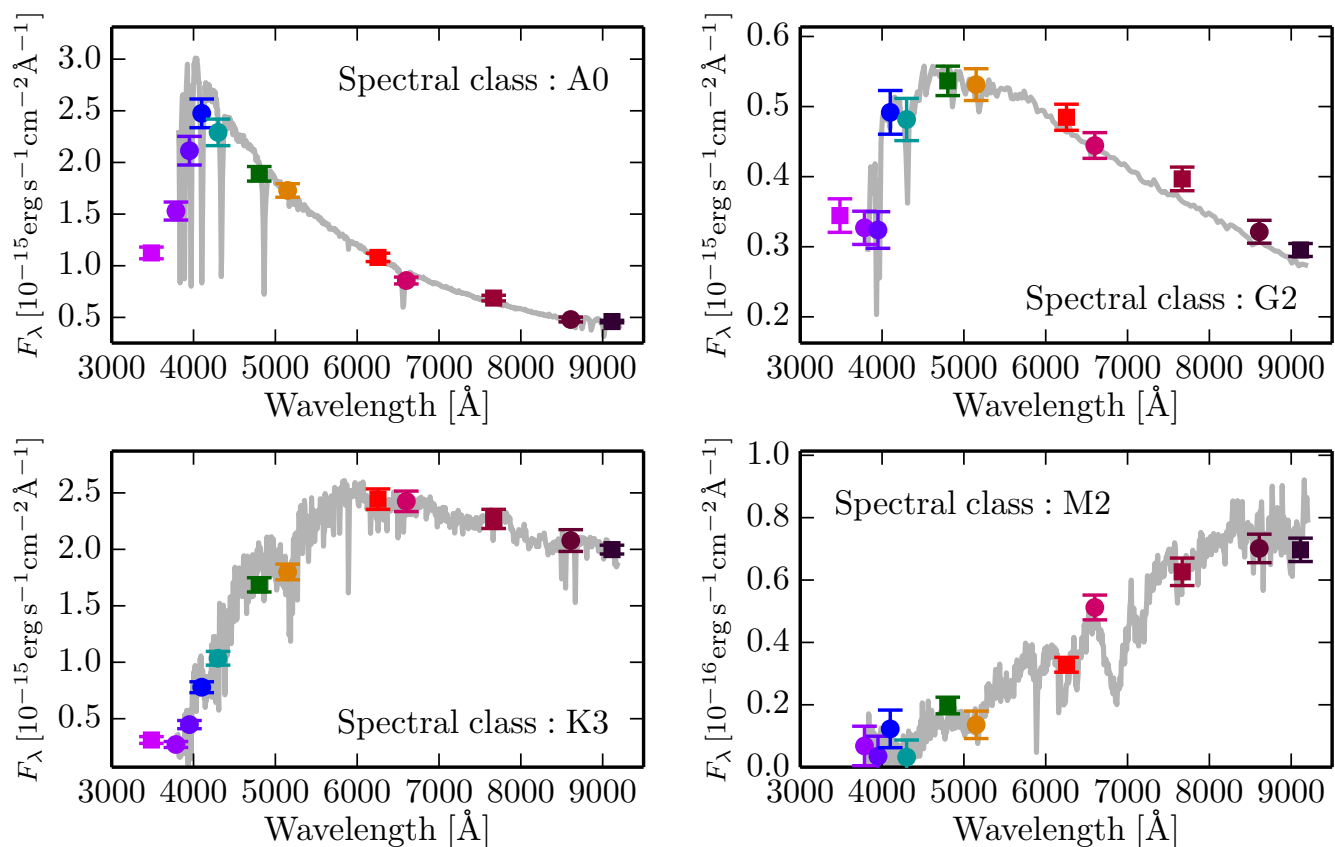


Fig. 9. J-PLUS photo-spectra of the four stars marked in Fig. 7. The gray lines show the SDSS spectra of these stars.

adopted in this case is the Boender-Timmer-Rinnoy Kan global algorithm (Boender & Stougie 1982). The model fluxes considers variations in effective temperature (T_{eff}), surface gravity ($\log g$) and metallicity ($[\text{Fe}/\text{H}]$). We perform tests using observations from the STIS Next Generation Spectral Library (NGSL; Gregg et al. 2006; Heap & Lindler 2007)¹⁶. After synthesizing J-PLUS photometry using the NGSL spectra and the filter responses, we attempt to recover the atmospheric parameters using the model grids and fitting techniques mentioned above. We focus our tests on the domain of the GK spectral types (3500–6000 K). Even under the assumption that the measurements of the J-PLUS filter responses are perfect, these tests should include systematic errors associated with the imperfections in the model atmospheres and spectral modelling.

The effective signal-to-noise per pixel of the observations in the library, most likely dominated for many stars by systematic errors (e.g., slit centering corrections), is expected to be in the range 20–50. When the fluxes are integrated over the J-PLUS’ passbands for the the signal-to-noise is increased by a large factor. The resulting, typical uncertainties in the recovery of the stellar parameters are 135 K in T_{eff} , 0.6 dex in $\log g$, and 0.4 dex in $[\text{Fe}/\text{H}]$. The stellar parameters of the stars in the library are not uniformly distributed like in the tests, but they are not heavily biased. Barring errors in the filter responses and our ability to correct for atmospheric extinction, we conclude that at least for signal-to-noise ratios lower than 50, i.e., 0.02 mag in the J-PLUS photometry, random errors will likely dominate the error budget. Note that these uncertainties are very close to those obtained when adopting the approach based upon ANNs.

¹⁶ See also the online document <https://archive.stsci.edu/pub/hlsp/stisngsl/aaareadme.pdf>

Thanks to the stellar temperature, metallicity, and gravity derived from J-PLUS photometry, a number of topics can be explored:

- *Search for metal poor stars.* With the exception of mass-transfer binaries or stars in advanced stages of evolution, long-lived low-mass, main sequence stars, in the absence of mass transfer interactions, retain in their atmospheres the chemical signature of their natal environments. As a result, the elemental abundances of ancient stars in the Galaxy provide the means to study the chemical evolution of the early Universe. The identification and subsequent detailed spectroscopic analysis of these old stars can provide crucial observational constraints for Galactic chemical-evolution models (Salvadori et al. 2010), as well as placing fundamental constraints on the first mass function.

Obtaining spectroscopic estimates of metallicity ($[\text{Fe}/\text{H}]$) is a costly endeavour, however, requiring pre-selection and follow-up medium-resolution spectroscopic analysis (Beers & Christlieb 2005). While there now exist tens of thousands of stars with well-measured metallicities below 1/100th of the solar value ($[\text{Fe}/\text{H}] < -2.0$), the numbers decrease rapidly with declining metallicity – less than 25 ultra metal-poor stars (UMP; $[\text{Fe}/\text{H}] < -4.0$) are known to date (Placco et al. 2015).

We have demonstrated that the J-PLUS photometric system permits detection of metal-poor stars across a wide range of temperatures, 4000–7000 K. When using ANNs, this range can be further extended by broadening the distribution of stars used to train the network, whether by making use of synthetic spectra or empirical template libraries (Kesseli et al. 2017). As photometry is obtained for lower metallicity

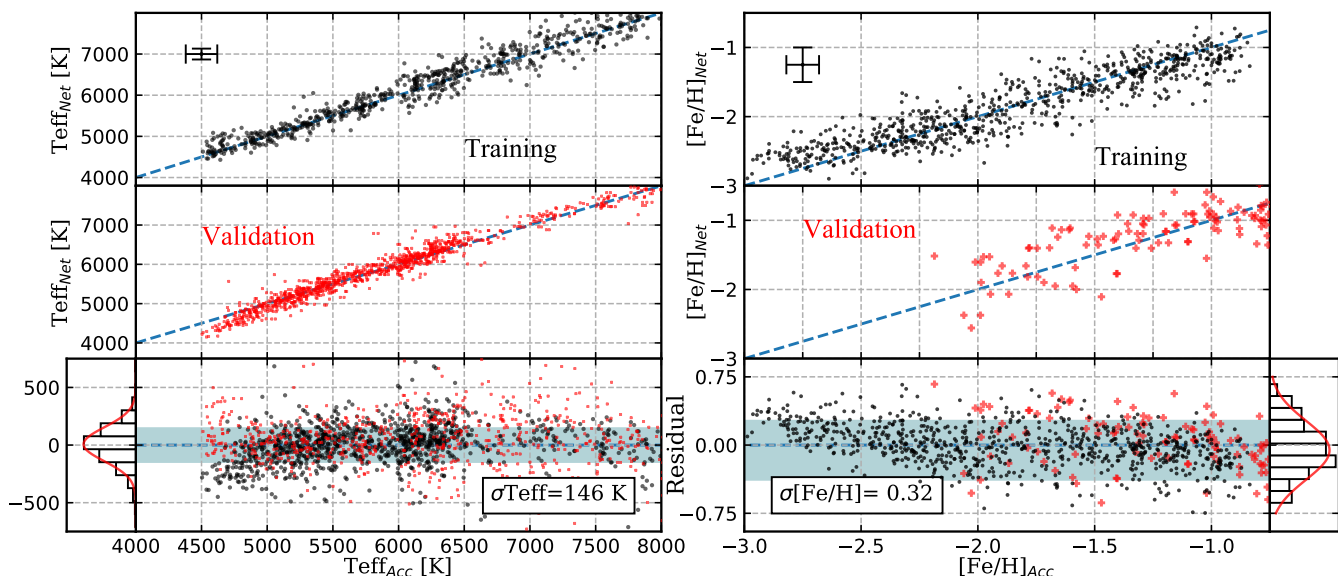


Fig. 10. *Left panel:* Surface temperature predictions for a subset of J-PLUS EDR. *Right panel:* Metallicity predictions for a subset of J-PLUS EDR. Both networks were trained synthetically, the results of which denoted by black dots. The networks were then tested on EDR photometric inputs, shown in red. Estimates are compared in both cases to accepted values from the SSPP. Maximum-likelihood gaussian fits, shown in red, were produced for the residuals of the EDR photometric estimates.

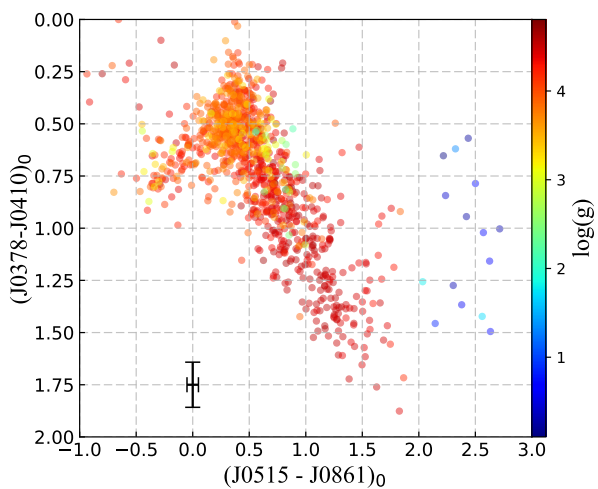


Fig. 11. Log g separation in a surface gravity sensitive J-PLUS color-color plot.

stars, calibration of estimates in the increasingly metal-poor regime ($[\text{Fe}/\text{H}] < 2.0$) will become possible using the methods described. It is anticipated that estimates of metallicity down to $[\text{Fe}/\text{H}] \sim -3.5$ will be achieved, which would represent a major improvement from previous broad-band photometric methods, where SDSS photometry reached saturation at $[\text{Fe}/\text{H}] < -2$ (e.g., Ivezić et al. 2008), or $[\text{Fe}/\text{H}] < -2.7$ (An et al. 2015).

- *Ultracool dwarfs.* Defined as dwarf stars with spectral types later than M6, they include both very low-mass stars and brown dwarfs. Three different approaches are being carried out to find ultracool dwarfs using J-PLUS data, which should

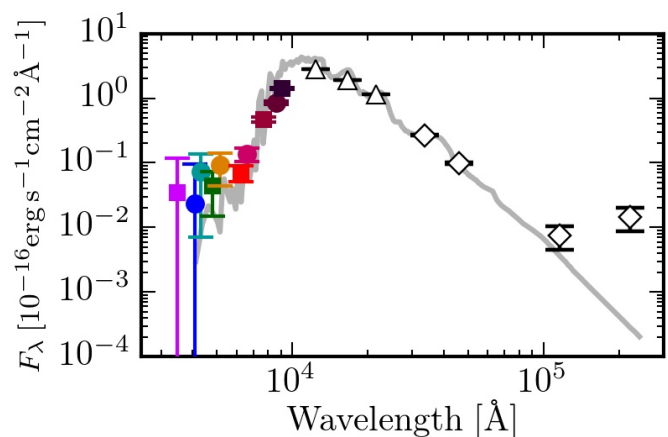


Fig. 12. J-PLUS photo-spectrum of a confirmed ultracool dwarf in the EDR footprint. J-PLUS measurements (coloured symbols) are complemented by 2MASS (white triangles) and WISE (white diamonds) data. The (smoothed) best fit model is provided by the grey line.

provide around 1 600–2 400 new candidates by the end of the survey:

1. *Photometric search.* A preliminary discriminator for candidate objects is built upon the subsample of spectroscopically confirmed M dwarfs with known spectral types (West et al. 2011) that count with J-PLUS photometry. The (J-PLUS based) $i - z$ color of those sources is used to search for candidates in the entire J-PLUS database. Using a Virtual Observer (VO) tool like VOSA (Bayo et al. 2008) we are able to obtain SEDs for those candidates, and provide estimates for their effective temperature (T_{eff}). Objects with effective temperatures corresponding to spectral types later than M6 (according to West et al. 2011) are flagged as can-

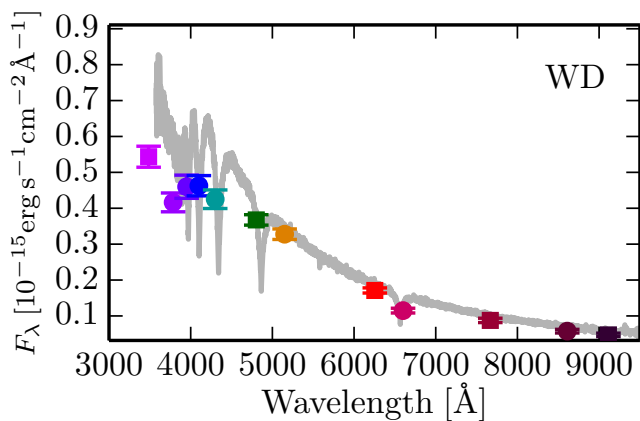


Fig. 13. J-PLUS photo-spectra of the white dwarf marked in Fig. 7. The gray lines show the BOSS spectra of this object.

didate ultracool dwarfs. Using *Aladin* (Bonnarel et al. 2000) we are able to identify the objects previously reported in the literature. One of these is shown in Fig. 12.

2. Kinematic search. Given that ultracool dwarfs are intrinsically faint objects, they must be located in the solar vicinity, and thus should have, on average, a high relative motion. Using the information available in *Simbad* (Wenger et al. 2000) we defined a limit in proper motion of 50 mas/y to distinguish between ultracool dwarfs and other types of objects with a high degree of completeness and low degree of contamination. Effective temperatures of the candidates ultracools will be subsequently computed using *VOSA*.

3. Search based on Artificial Intelligence techniques. Using the J-PLUS color combinations that best reproduce SED shapes, different approaches will be used to identify new ultracool dwarfs.

- *Detection and characterization of white dwarfs.* The bluest J-PLUS bands permit to characterize the white dwarf (WD) population. As example, we present the J-PLUS photo-spectra of a spectroscopically confirmed WD in Fig. 13. From the experience from the Sloan and the Gaia surveys, we expect that J-PLUS will characterise around 3 WDs per square degree, or about 30 000 WDs for a final area of 8 500 deg².
- *Search for stellar streams in the MW halo.* The efficiency of detecting stellar streams in the MW halo is heavily dependent on the possibilities to filter out candidate sub-populations from the background halo stars, which in general have very similar properties, also being old, low in mass, and poor in metals. While already the SDSS broad-band filters have allowed to search for and detect stellar streams using the Hess diagrams (Grillmair & Dionatos 2006), the stellar parameters based on the J-PLUS filter set are even more promising for such a work, especially in combination with the powerful but shallower dataset of stellar kinematics from the Gaia mission.

4.1.2. Searching for planetary nebulae and symbiotic stars

Here we address the study of distinct families of systems, namely planetary nebulae (PNe) and symbiotic systems (SySts), the reason being that both involve the ionization of circumstellar gas, either ejected and ionized by a white dwarf itself (PNe), or associated to the stellar wind of a red giant that is ionized by high

energy photons generated in the accretion onto a companion star (SySts).

PNe are essential objects to study the chemical evolution of galaxies (see, for a review, Magrini et al. 2012) as well as to determine extragalactic distances (see, for instance, Ciardullo 2012). On the other hand, the binary nature of the symbiotic systems make them one of the possible supernova Ia progenitors (Whelan & Iben 1973; Di Stefano 2010; Dilday et al. 2012). Both enrich the interstellar medium, with PNe providing important information about the stellar nucleosynthesis of low- to intermediate-mass stars (0.8–8 M_⊙). However, both families of objects are intrinsically different, with SySts constituting interacting binary systems which can alter significantly the evolutionary and chemical path of the stars involved.

A continuum marked by emission lines is the optical fingerprint of PNe while this is the historical definition and usual way to identify SySts. In fact, the PNe and the population of known SySts revealed in optical surveys usually present strong hydrogen and helium recombination lines (e.g., H α , He II) as well as a number of low- and high-excitation lines (e.g., [O III], or even [Fe V] and [O VI] in the case of SySts). They are thus ideal targets to be searched for by J-PLUS in the direction of the north Galactic halo. Moreover, SySts’ spectra (see, for instance, Munari & Zwitter 2002) are also rich in absorption features, like TiO, VO and others, due to the presence of the cool companion (with M, K or G spectral types).

Despite the strong efforts to increase the number of Galactic PNe presently known (~3000, Parker et al. 2012), only 14 of them are classified as halo PNe (HPNe; Otsuka et al. 2015). Nevertheless, more PNe are certainly hidden in the Galactic halo, since the mass range of PNe (SySts) dominates the halo stellar population. Regarding SySts, 251 are known in our Galaxy, and only 5 % of those are located in galactic latitudes of $|b| > 30$ deg, (Akras et al., submitted).

Given the scarcity of PNe and SySts in the Galactic halo, we aim at performing the first systematic search of these evolved objects, at high latitudes, by using the 12 J-PLUS filters. These twelve measurements provide a number of colour combinations by far more numerous than those used in any previous search (for instance in IPHAS, Drew et al. 2005; or VPHAS, Drew et al. 2014), making it much easier to distinguish PNe and SySts with strong emission lines from other emission line objects in the optical. In Fig. 14 we show that J-PLUS is able to optimally separate different families of emission line objects. In particular, we reproduce the equivalent IPHAS $r'-H\alpha$ vs. $r'-i'$ colour-colour diagram, which in IPHAS as well as in our survey can efficiently highlight and discriminate the HPNe locus with respect to their mimics. The IPHAS version of this diagram is found in Fig. 1 of Viironen et al. (2009). Other combinations of colours have been explored for J-PLUS (Gutiérrez-Soto et al., in prep.). For instance, the $g-J0515$ vs. $J0660-r$ diagram, in Fig. 14, is also found to provide a good PNe(SySts) discrimination.

In order to build these diagrams, J-PLUS synthetic magnitudes were computed for different kinds of objects (as given in the caption and legend of Fig. 14). These synthetic data were obtained by means of observed spectra and a grid of models for HPNe provided by the photo-ionization code *CLOUDY* (Ferland et al. 2013). In addition, the J-PLUS SVD of two known HPNe (H 1-4 and PNG 135.9+55.9) are presented in Fig. 14. This figure shows that the locus occupied by the two HPNe observed by J-PLUS SVD is compatible with that associated with the synthetic data. In the case of PNG 135.9+55.9, the uncertainties of the spectroscopic data constitute the lower limits for the errors associated to the intensities of the important lines within each

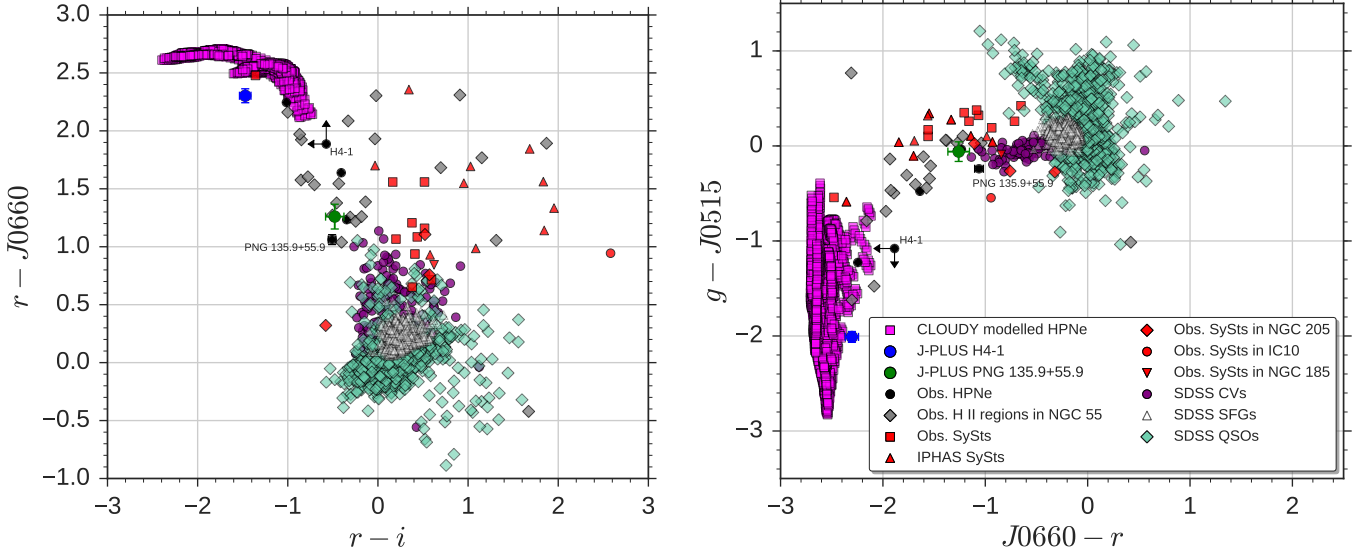


Fig. 14. *Left panel:* J-PLUS r - $J0660$ vs. $r - i$ colour-colour diagram, equivalent to IPHAS $r' - H\alpha$ vs. $r' - i'$. *Right panel:* $g - J0515$ vs. $J0660 - r$ diagram. Blue and green symbols with errorbars are the J-PLUS observations for H 4-1 and PNG 135.9+55.9, respectively. Included in the diagrams are families of CLOUDY modelled HPNe (pink boxes) spanning a range of HPNe properties. Black circles represent HPNe H 4-1 and PNG 135.9+55.9 spectra from SDSS, DdDM-1 (Kwitter & Henry 1998), NGC 2022 (Kwitter et al. 2003), and MWC 574 (Pereira & Miranda 2007). Gray diamonds represent H II regions in NGC 55 (Magrini et al. 2017). Red boxes display Munari & Zwitter (2002) SySts and red triangles correspond to IPHAS symbiotics (Rodríguez-Flores et al. 2014). Red diamonds, circles and inverted triangles refer to the SySts in external galaxies, NGC 205 (Gonçalves et al. 2015), IC 10 (Gonçalves et al. 2008) and NGC 185 (Gonçalves et al. 2012), respectively. Violet circles correspond to SDSS cataclismic variables (CVs). Black, empty triangles refer to SDSS star-forming galaxies, SDSS SFGs. SDSS QSOs at different redshift ranges (light blue diamonds) were selected, since some of their lines are mimics of the $H\alpha$ and/or $[O III] 500.7$ nm emission in the local Universe.

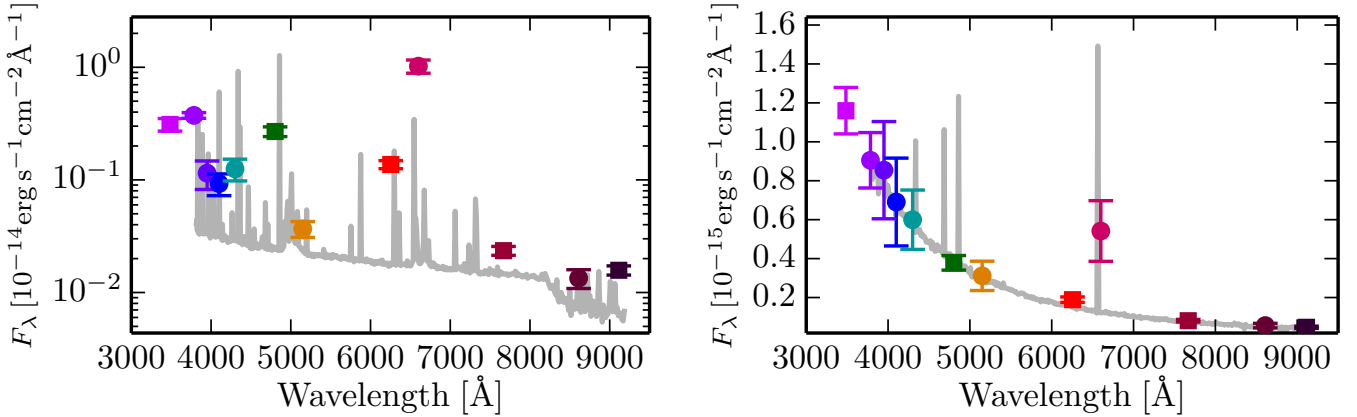


Fig. 15. J-PLUS photo-spectra of the PNe H 4-1 (*left panel*) and PNG 135.9+55.9 (*right panel*). In both spectra the strong $H\alpha$ emission is easily perceptible.

filter (Richer et al. 2002). In regard of H 1-4, we need to point out that the SDSS spectrum is saturated in $[O III] 5007 \text{ \AA}$ as well as in $H\alpha$. Hence, the synthetic J-PLUS $J0660$, r , $J0515$ and g magnitudes are either upper or lower limits, as indicated in the colour-colour diagrams. Moreover, we note that H 1-4 is found to lie very close to the regime where halo PNe are expected to be, while the PNG 135.9+55.9 lies rather farther away, in the regime of H II regions. This happens because the PNe in the diagrams have different excitation degrees, and those of lower-excitation are, photometrically, indistinguishable from H II regions. Only the inclusion $He II 4686 \text{ \AA}$ magnitudes could avoid this problem. Fortunately, only a few Galactic H II regions will be detected by J-PLUS, whose observations will be towards the halo, while massive and young stars are typically in the disk. In Fig. 15 we

present the J-PLUS photo-spectra of these two HPNe, in which the $H\alpha$ emission line is easily perceptible.

Machine learning algorithms such as linear discrimination analyses and classification trees, among others, will be applied to this work in order to find more general ways to discriminate PNe and SySts from other strong emission-line sources that will be observed by the J-PLUS survey.

As for the case of SySts candidates, additional clues can also be provided from observations available in X-rays surveys (e.g., XMM-Newton, Chandra, and Swift), especially for the cases displaying weak emission lines (Mukai et al. 2016) and that can represent a significant fraction of SySts that have remained invisible to optical surveys up to present days.

4.1.3. Galactic Globular Clusters: the case of M15

The wide-field capabilities of JAST/T80Cam are an excellent tool to study a wide-range of integrated properties of Galactic globular clusters, such as mass and luminosity segregation, luminosity functions, and total mass, among others. In addition, the data can also be used to search for multiple populations¹⁷ in different regions of the clusters, as well as any large scale effects that may be related to them, such as disruption seen in the form of tidal tails. We expect to find around 10 globular clusters falling in the footprint of J-PLUS.

M 15 (NGC 7078) is an old (≥ 10 Gyr) and very metal-poor, $[\text{Fe}/\text{H}] = -2.3$, (Carretta et al. 2009), globular cluster, located ~ 10 kpc away from the Sun and the Galactic centre (Harris 2010). Interestingly, a previous Hubble Space Telescope (HST) analysis (Larsen et al. 2015) indicated a split in the lower Red Giant Branch (RGB) stellar distribution, with first and subsequent generation populations dominating at different cluster-centric distances. To illustrate this science case, M 15 has been observed during J-PLUS science verification well beyond the tidal radius ($R_{\text{tidal}} = 21.5$ arcmin, Harris 2010) with uniform photometry. The full analysis for this cluster using J-PLUS SVD is presented in Bonatto et al. (2018).

Because of crowding, Bonatto et al. (2018) employ IRAF/Daophot to build photometric catalogs for the 12 bands of the whole M15 field. Calibration is performed with the zero-points provided by the UPAD. Here we aim to emphasize the potential of J-PLUS on the analysis of globular clusters, particularly with respect to detecting multiple stellar populations in the RGBs of M15. An excellent example is the colour-magnitude diagram (CMD) $J0378$ versus $(J0378 - J0861)$ shown in Fig. 8 of Bonatto et al. (2018), in which the RGB appears to split into two sequences. The splits are considerably wider than the ones expected from photometric scattering, as can be inferred from the average error bars. Fiducial lines, built to represent the mean path followed by each sequence, are included in that figure as a visual aid. Visually considering the sequence split and guided by the fiducial lines, Bonatto et al. (2018) separate the stars in blue and red sub-samples, and take their magnitudes in the other J-PLUS filters, noticing that the split vanishes when broad-band filters such as g and r are considered. This suggests a relation to light-element abundance differences, since $J0378$ and $J0861$ are sensitive to N and Ca abundances. See Bonatto et al. (2018) for full details on this particular science case.

4.2. Studies in the nearby Universe

Large spectroscopic surveys of galaxies fail to map, at low redshifts, the whole extent of spatially resolved galaxies and their close environment. To solve the first issue, systematic studies based on integrated field units (IFUs) have been conducted (e.g., the Sauron project, de Zeeuw et al. (2002); ATLAS^{3D}, Cappellari et al. 2011; CALIFA, Sánchez et al. 2012; SAMI, Croom et al. 2012; MaNGA, Bundy et al. 2015). With these, one can analyze galaxies as a whole and look for gradients or trends in specific properties. However, while spectroscopy is usually less efficient and more time consuming than photometric studies, IFU studies tend to be limited to bright and size-selected objects.

Half-way between classical photometry and spectroscopy, J-PLUS will build a formidable legacy data set by delivering low resolution spectroscopy for every pixel over a large, con-

tiguous area of the sky. This IFU-like character, allowing a 2D pixel-by-pixel investigation of extended galaxies, will lead to much larger galaxy samples than classical multi-object spectroscopic surveys. In addition, no sample selection criteria other than the photometric depth in the detection band will result in a uniform and non-biased spatial sampling, thus allowing for environmental studies. Furthermore, provided that direct imaging is more efficient than spectroscopy, J-PLUS will be generally deeper than traditional spectroscopic studies, enabling better access to galaxy outskirts and fainter companions.

Figure 17 shows the limits of J-PLUS for studies in the nearby Universe. This figure represents the location of the EDR galaxies ($\text{MORPH_PROB_STAR}^{18} < 0.2$) in the plane defined by the mean effective surface brightness $\langle \mu_{e,r} \rangle$ and the apparent magnitude r , both in the r -band. Note that down to $r = 20.5$ J-PLUS can detect galaxies brighter than $\langle \mu_{e,r} \rangle = 25.0$. In addition, objects down to $r = 22.0$ have been observed by J-PLUS with $\langle \mu_{e,r} \rangle$ brighter than ≈ 23.5 . This depth makes to J-PLUS an ideal survey to select targets for spectroscopic follow-ups by future surveys such as WEAVE¹⁹, MANGA²⁰, or DESI²¹, among others.

J-PLUS will also constitute a reference survey in the optical, due to its unique color information, in cross-correlation studies with surveys in other wavelengths, such as the IR, X-rays or γ rays. The study of energetic sources by missions like XMM²², Chandra²³, Swift²⁴, Suzaku²⁵ or Fermi²⁶ will be complemented by the multi-color information provided by J-PLUS, which should be of particular relevance in the local universe.

In this section, we demonstrate J-PLUS capabilities to study the properties of nearby galaxies, focusing on their photometric redshift (Sect 4.2.1), 2D star formation rate (hereafter SFR, Sect 4.2.2), 2D stellar content (Sect 4.2.3), and environment (pairs, groups, and clusters; Sect 4.2.4).

4.2.1. Photometric redshifts

A photo- z is an estimate of the redshift of an extragalactic source based upon its SED as it is inferred from its apparent magnitudes provided by a particular filter system. From its first application in the 1960s (Baum 1962), the estimation of photo- z s has experienced a very significant evolution. Nowadays, photo- z s have become an essential tool in modern astronomy since they represent a quick and almost inexpensive way of retrieving redshift estimates for a large amount of galaxies in a reasonable amount of observational time.

Although redshift estimations from galaxy colours are more uncertain than those obtained directly from a spectrum, this situation is certainly being mitigated. The strong dependency between the wavelength resolution (number and type of pass-bands) and the achievable precision of photo- z estimates (e.g. Hickson et al. 1994; Benítez et al. 2009) has inspired the design

¹⁸ This flag is found in the database table `jplus.stargalclass` and provides the probability of an object for being a star based upon morphological arguments. See López-Sanjuan et al. (2018) for further details.

¹⁹ <http://www.ing.iac.es/weave/>

²⁰ <http://www.sdss.org/surveys/manga/>

²¹ <http://desi.lbl.gov>

²² <http://sci.esa.int/xmm-newton/>

²³ http://chandra.harvard.edu/about/axaf_mission.html

²⁴ <https://swift.gsfc.nasa.gov>

²⁵ <https://www.nasa.gov/content/suzaku-mission-overview>

²⁶ <https://fermi.gsfc.nasa.gov>

¹⁷ Multiple stellar populations have been detected in a large fraction of galactic globular clusters (see e.g. Gratton et al. 2012, Bastian 2015).

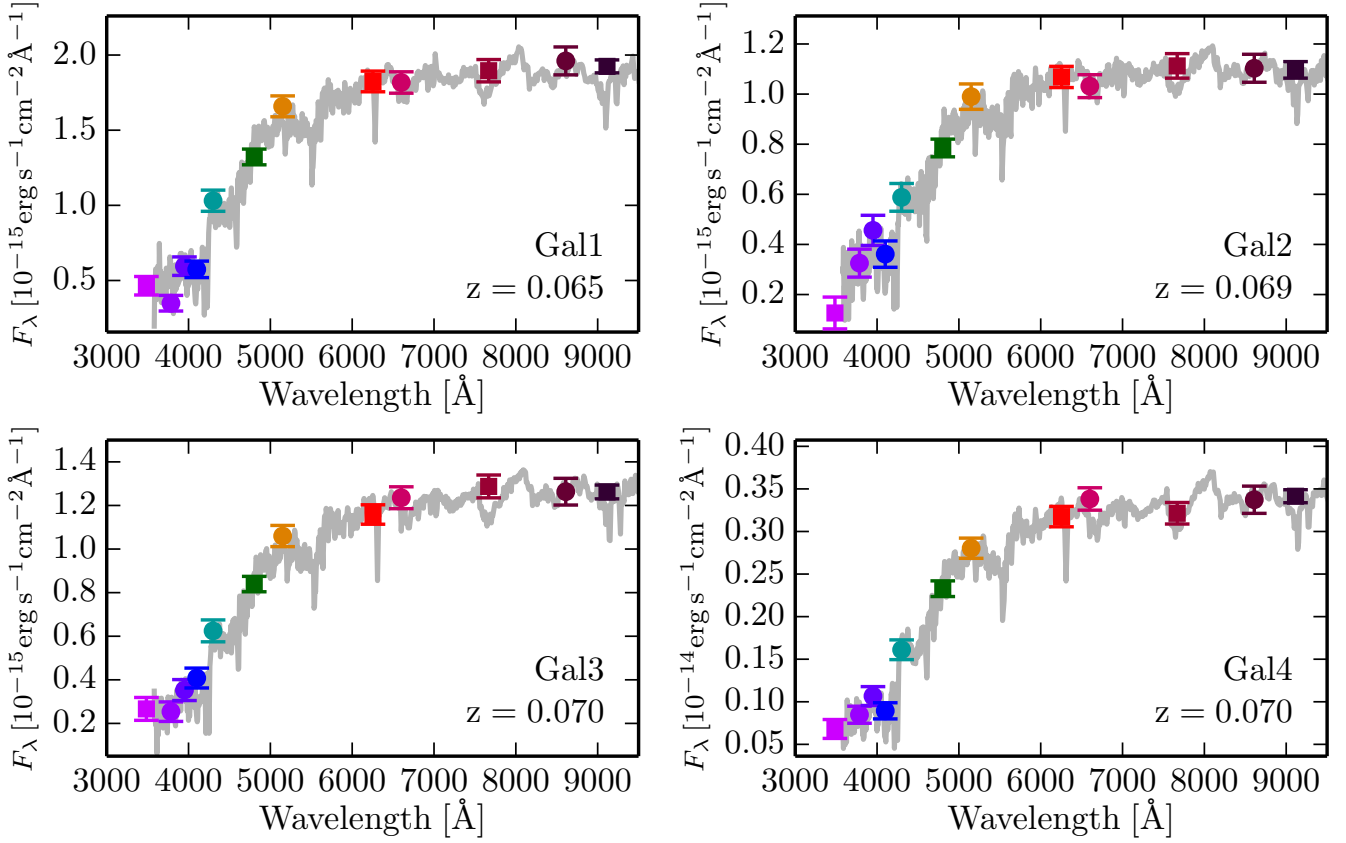


Fig. 16. J-PLUS photo-spectrum of the four galaxies marked in Fig. 7. The SDSS spectra, scaled to match the r band total magnitude from J-PLUS, are presented in grey.

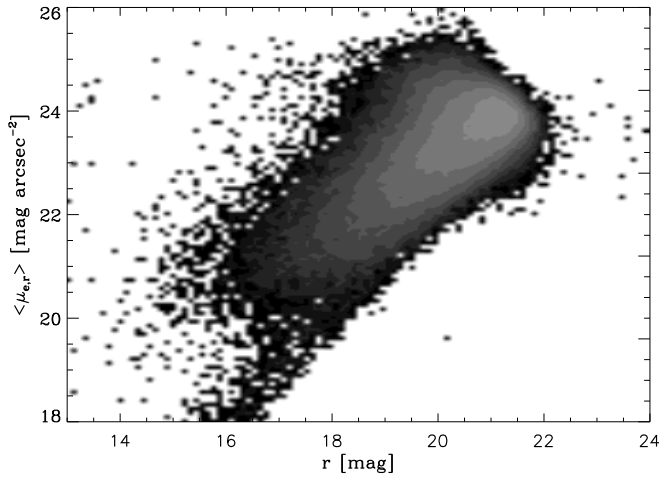


Fig. 17. Location of EDR galaxies in the plane defined by mean effective surface brightness $\langle \mu_{e,r} \rangle$ and apparent magnitude, both in the r band.

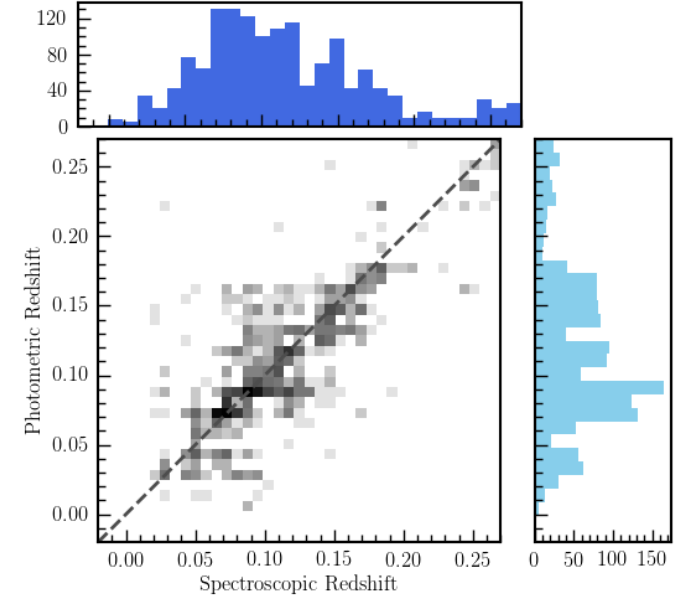


Fig. 18. J-PLUS photometric redshifts vs SDSS spectroscopic redshifts for the common sources in the J-PLUS EDR. The side panels show the projection in redshift space of the photometric (*right*) and spectroscopic (*upper*) values.

of a whole generation of medium-to-narrow multi-band photometric redshift surveys. Surveys such as COMBO-17, COSMOS, ALHAMBRA or SHARDS have used a combination of broad, medium and narrow-band filters to increase the sensitivity to emission-lines with moderate equivalent widths, providing photo- z estimates as accurate as $\delta_z/(1+z) < 0.01$ for high signal-to-noise galaxies. As demonstrated in Benitez et al. (2014b), the upcoming new generation of > 50 narrow-band photometric surveys will push this technique yet further, reaching a photo- z pre-

cision level of $\delta_z/(1+z) \sim 0.003$ or 0.3 %, equivalent to a resolution of $R \simeq 50$ from a real spectrograph.

The main uncertainties in the estimation of photo- z s for optical surveys such as J-PLUS come from i) the available

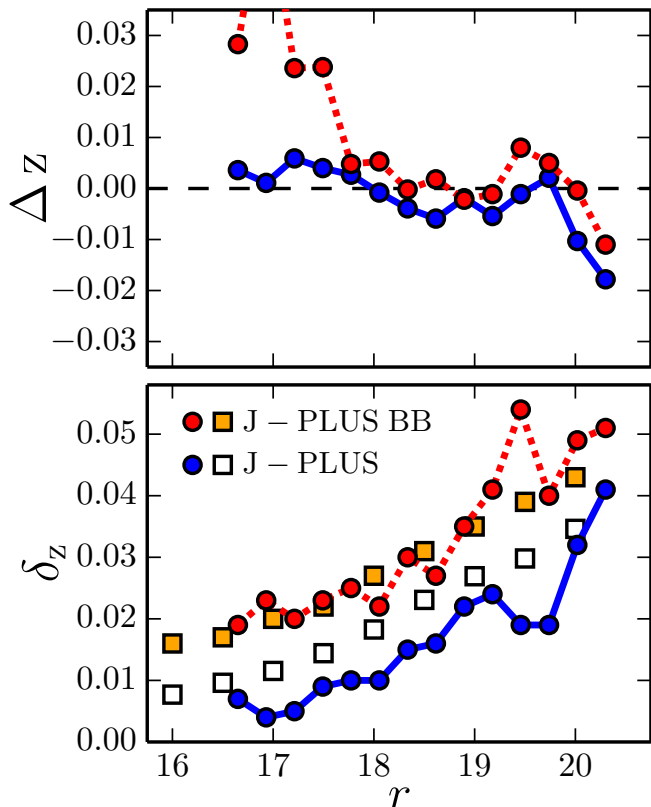


Fig. 19. J-PLUS photometric redshift bias (*top panel*) and precision (*bottom panel*), estimated from EDR data. The blue circles show the results with the twelve J-PLUS filters, and the red circles with only the *ugriz* broad bands used. The orange (five bands) and white (twelve bands) squares show the expected photo- z precision from the realistic simulations in Molino et al. 2018.

wavelength resolution (number and type of pass-bands), and ii) the limited photometric depth of the observations. The J-PLUS photometric system is well designed to recover accurate photo- z information of nearby galaxies with $z \lesssim 0.2$, thanks to continuous covering of the 4000 Å break and the presence of particular emission lines. We address the issue of photo- z estimation in J-PLUS data by comparing photo- z estimates from EDR with spectroscopic redshifts from the literature, in particular from SDSS and from the nearby clusters A2589 & A2593 (located at $z \sim 0.043$, see Sect. 4.2.4 and Molino et al. 2018 for further details). We also compare our photo- z estimates with the “real” redshifts of synthetic, realistically simulated J-PLUS sources injected in real J-PLUS images, (Molino et al. 2018). The codes used in this analysis are BPZ²⁷ and LePhare²⁸.

Let us first introduce a representative example of J-PLUS photo-spectra for four cluster galaxies located at $z \sim 0.065$ in the EDR tile 4951, see Fig. 16. These nearby photo-spectra are found to be in good agreement with the outputs from spectroscopy (grey lines). We next present a quantitative comparison between J-PLUS EDR photo- z s and SDSS spectroscopic values in Fig. 18. We find that the spectroscopic values are retrieved with no significant bias ($|\Delta z| \equiv |z_{\text{phot}} - z_{\text{spec}}| < 0.005$ for r -band magnitude < 20), and

²⁷ <http://www.stsci.edu/~dcoe/BPZ/>

²⁸ <http://www.cfht.hawaii.edu/~arnouts/LEPHARE/lephare.html>

a typical error δz in the range 0.005–0.04 for $r \in [16, 20.5]$. These results are in agreement with those from Molino et al. (2018) in two nearby clusters contained in the J-PLUS SVD. The explicit dependence of the photo- z bias and precision with the r -band magnitude is shown in Fig. 19. As expected, the quality degrades at lower signal-to-noise, reaching $\delta z \sim 0.03$ at $r \sim 20$. We stress that photo- z precision below 1% is reached for galaxies brighter than $r = 18$. We also stress the good agreement with the predictions from the simulations of Molino et al. (2018) (displayed by squares in Fig. 19).

Finally, the benefit of extending the classical five broadband surveys (such as SDSS) to twelve bands including medium width and narrow filters is also shown in Fig. 19. Both the direct comparison with SDSS spectroscopic information and the simulations from Molino et al. (2018) found a significant improvement in the photo- z precision at all magnitude bins. This reaches a factor as high as 2.5 gain when the signal-to-noise in the narrow-band filters is large enough. Interestingly, as pointed out in Molino et al. (2018), the SDSS-like surveys cannot surpass a certain precision in the photo- z estimates irrespectively of the signal-to-noise of the galaxies. This limitation is imposed by the poor wavelength resolution provided by broadbands, causing a degeneracy in the colour-redshift space. Although J-PLUS observations are fainter in terms of photometric depth to those of SDSS, they are indeed deeper in terms of photometric redshift depth, due to the addition of the seven narrow-bands to the filter system.

4.2.2. 2D SFR

As an alternative to spectroscopy, narrow-band filters offer a great opportunity to conduct systematic studies of ELGs, sacrificing the precision that spectroscopy offers for much larger data samples with significantly better statistics. The SFR is known to correlate with the emission of $H\alpha$ by the heated gas in star-forming regions (Kennicutt 1998). Thanks to the large sky coverage and the specific rest-frame $H\alpha$ filter *J0660*, J-PLUS is a very powerful survey to study the integrated and the spatially resolved SFR at $z < 0.015$.

The work of Vilella-Rojo et al. (2015) describes an optimized methodology to extract the $H\alpha$ flux and the SFR from J-PLUS-like photometric data. First, the $H\alpha + [\text{N II}]$ flux covered by the *J0660* filter is isolated by subtracting an underlying continuum estimate. This estimation is produced by a SED-fitting technique that uses all the available J-PLUS filter set. After that, the dust extinction is corrected for and the $[\text{N II}]$ flux removed using empirical relations derived from the SDSS spectroscopic sample. We test the above procedure with synthetic photometry derived from the SDSS spectra of star-forming regions, and find that the measured $H\alpha$ flux is unbiased. This is in contrast with usual methods based solely on *J0660* – r information, which underestimate measurements of $H\alpha$ fluxes by $\sim 20\%$ (Vilella-Rojo et al. 2015).

We also check this procedure based on synthetic photometry with J-PLUS SVD and EDR, as presented in Logroño-García et al. (2018). We compare the $H\alpha$ flux measured with J-PLUS photometry against spectroscopic measurements from SDSS and CALIFA in 46 shared HII regions. We find that the J-PLUS $H\alpha$ flux is consistent with the spectroscopic one, with a median flux ratio $R = F_{H\alpha}^{\text{J-PLUS}} / F_{H\alpha}^{\text{spec}} = 1.01 \pm 0.04$ (Logroño-García et al. 2018). This demonstrates the capabilities of the J-PLUS filter set and validates the methodology presented in Vilella-Rojo et al. (2015).

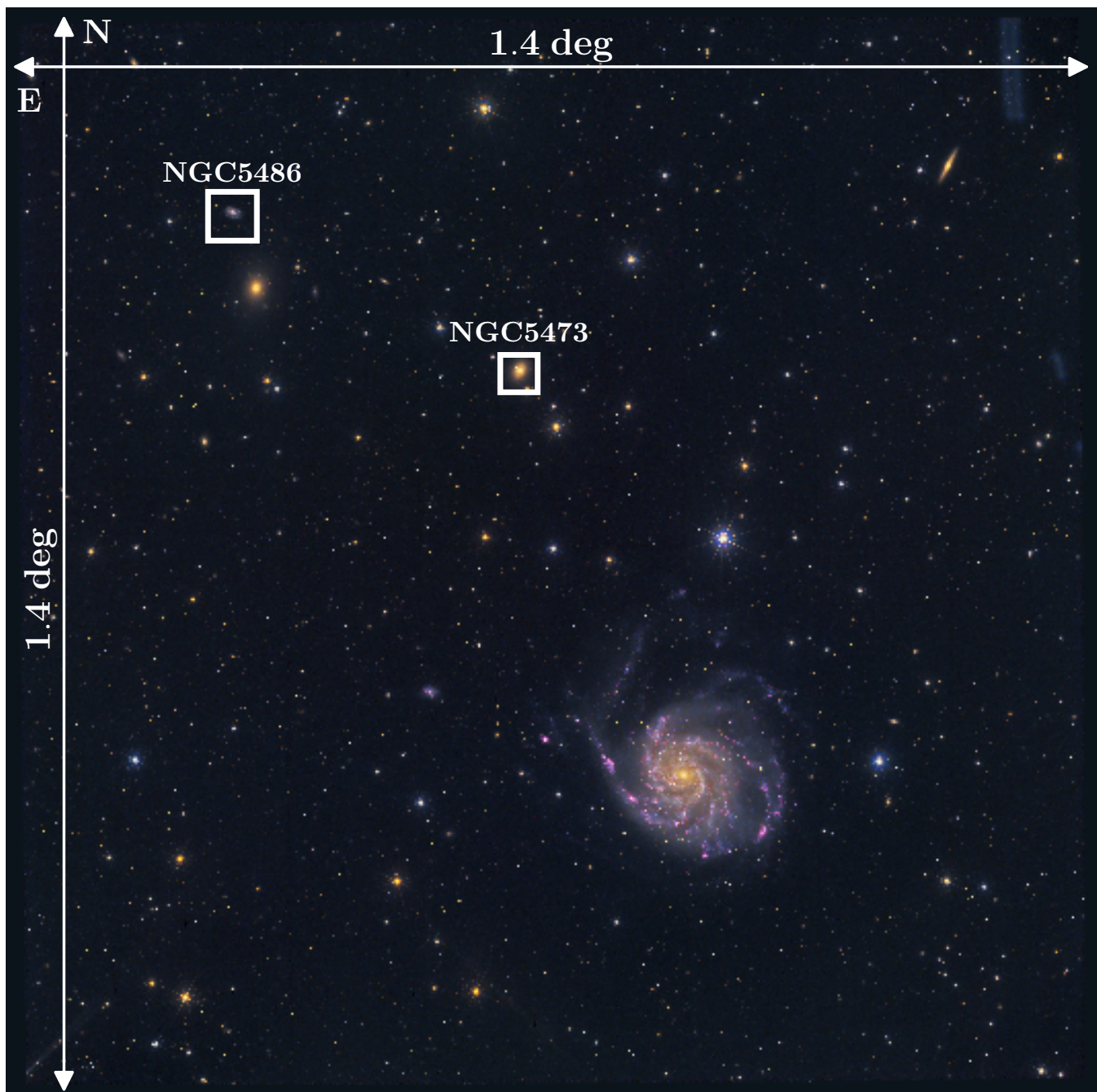


Fig. 20. One of the J-PLUS SVD pointings, including M101 and several NGC galaxies, two of which are indicated in white boxes as they are discussed in this paper.

The M101 J-PLUS SVD field is presented in Fig. 20. In addition to M101, other nearby galaxies are presented in the field, such as the elliptical galaxy NGC5473 (see Sect. 4.2.3) and the star-forming galaxy NGC5486. To illustrate J-PLUS potential on the study of $H\alpha$ emission, we present the study of one NGC5486 HII region in Fig. 21. J-PLUS photometry at the location of the SDSS fibre is consistent with the SDSS spectra, and presents a clear flux excess in the $J0660$ band due to the $H\alpha + [N II]$ emission of the region. The ratio between the J-PLUS and the spectroscopic $H\alpha$ flux is $R = 0.86 \pm 0.18$, i.e., compatible with unity. Moreover, the $J0378$ band is also raised because of the nebular $[O II]$ emission. This line is outside the SDSS spectral cov-

erage at $z < 0.015$, while J-PLUS provides valuable information for systematic $[O II]$ studies in the nearby Universe. Finally, the J-PLUS $J0660 - r$ image of NGC5486 shows a population of HII regions lacking spectral information. The study of spatial gradients within those galaxies, together with individual HII regions in a large, nearby galaxy sample will be possible after J-PLUS completion. As a bonus, it will also be possible to address the impact of the environment on those systems.

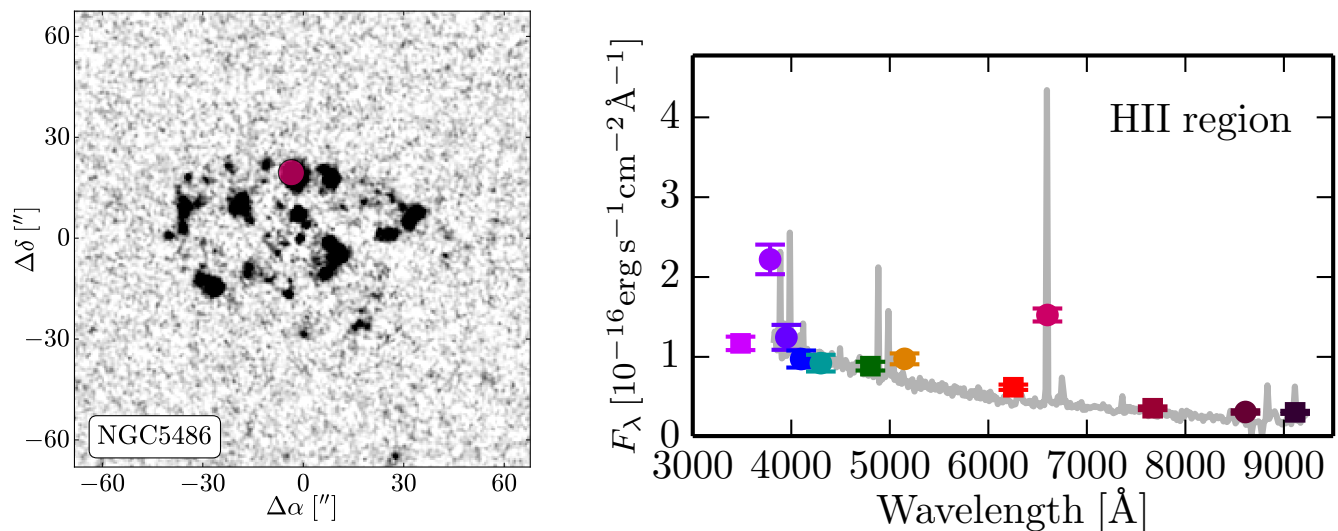


Fig. 21. NGC5486 as seen in the J-PLUS $J0660 - r$ image (*left panel*). The panel shows a 53.3 arcmin^2 area. The red dot marks the position of a HII region observed spectroscopically by SDSS. The J-PLUS photo-spectrum and the SDSS spectrum of such region are shown in the *right panel*. The data sets are normalized to have the same r -band magnitude. The $J0660$ and $J0378$ fluxes are raised because of the $H\alpha$ and $[\text{O II}]$ nebular emission.

4.2.3. 2D stellar populations

The spatial variations of stellar population properties within a galaxy are intimately linked to their formation process. Therefore, spatially resolved studies of galaxies are critical to uncover the history of formation and assembly of local galaxies. Although the arrival of integral field spectroscopy (IFS) surveys constitutes a significant breakthrough in the field, recent techniques that combine photometric multi-filter surveys with spectral fitting diagnostics have opened a new way to disentangle the stellar population of unresolved extended galaxies, and with a relatively low-cost compared to IFU surveys.

Current generations of IFS surveys allow detailed internal analyses through multiple spectra of each galaxy by creating a 2D map of the object. While these surveys are very powerful, there are still limitations in terms of accessible redshift ranges and galactocentric distances. For example, MaNGA aims to obtain spatially resolved spectroscopy of 10 000 galaxies but it will be limited to resolve galaxies spatially out to $R = 1.5 R_{\text{eff}}$ ²⁹ (with a subsample reaching $R = 2.5 R_{\text{eff}}$), and with a median redshift of $z \sim 0.03$. For the SAMI survey, redshifts are limited to $z < 0.095$ and the data typically reaches $1.7 R_{\text{eff}}$ ($2 R_{\text{eff}}$ for 40 % of the sample).

San Roman et al. (2018a) developed a technique to analyze unresolved stellar populations of spatially resolved galaxies based on photometric multi-filter surveys. They derived spatially resolved stellar population properties and radial gradients by applying a Centroidal Voronoi Tessellation and performing a multi-color photometry SED fitting (Díaz-García et al. 2015). The method has been tested and validated on a sample of 29 early-type galaxies observed by ALHAMBRA survey using 23 medium filter bands at the 3.5 m telescope of Calar Alto observatory. This observing technique enables spatially resolved stellar population studies out to considerably fainter surface brightness levels that are not possible with current IFU surveys. It also allows studies of very nearby galaxies ($z < 0.01$) that are so spatially extended to be unsuitable for the small FoV of current

IFU surveys. In this context multi-filter surveys open a way to improve our knowledge of galaxy formation and evolution that complements standard multi-object spectroscopic surveys.

In order to explore the IFU-like potential of J-PLUS, we have applied the previous multi-filter technique to two galaxies in common with CALIFA. As an illustrative example, Fig. 22 presents the age, metallicity and extinction maps of the elliptical galaxy NGC5473. Detail inspection of the 2D maps and the radial profiles show a flat age gradient and a mild negative metallicity gradient (i.e., the inner part is more metal-rich than the outer part of the galaxy). These results are in agreement with previous long-slit analysis (e.g., Sánchez-Blázquez et al. 2006, 2007; Spolaor et al. 2010), and also with the most recent IFU studies (e.g., Kuntschner et al. 2010; Wilkinson et al. 2015; Goddard et al. 2017). A detailed analysis, including a one-to-one comparison with different IFU techniques, is presented in a companion paper (San Roman et al. 2018b).

4.2.4. Environmental studies in the nearby Universe

One of the main strengths of large-area photometric surveys is the continuous information provided across the field. This enables the analysis of environmental effects, ranging from close pairs and nearby interactions to clusters and large scale structure.

The photometric redshift accuracy reached by J-PLUS in the nearby universe, with an uncertainty level $\delta_z \sim 0.02$ (Sect. 4.2.1), will improve our knowledge about local groups and clusters, and about their galaxy members. The potential of J-PLUS in this topic is demonstrated in Molino et al. (2018), where J-PLUS SVD of the two nearby galaxy clusters A2589 ($z = 0.0414$) and A2593 ($z = 0.044$) are analysed. Three JAST/T80Cam pointings were required to observe both clusters and the region between them, since they are separated by 3.5 deg on the sky. The photometric redshifts measured with BPZ2 are consistent with the EDR estimations presented in Sect. 4.2.1, as well as with the J-PLUS forecast based on the simulations performed by Molino et al. (2018). The empirical redshift probability distribution functions (PDFs) can be used to look for poten-

²⁹ The effective radius R_{eff} is defined as the radius containing half of the total light emitted by the galaxy.

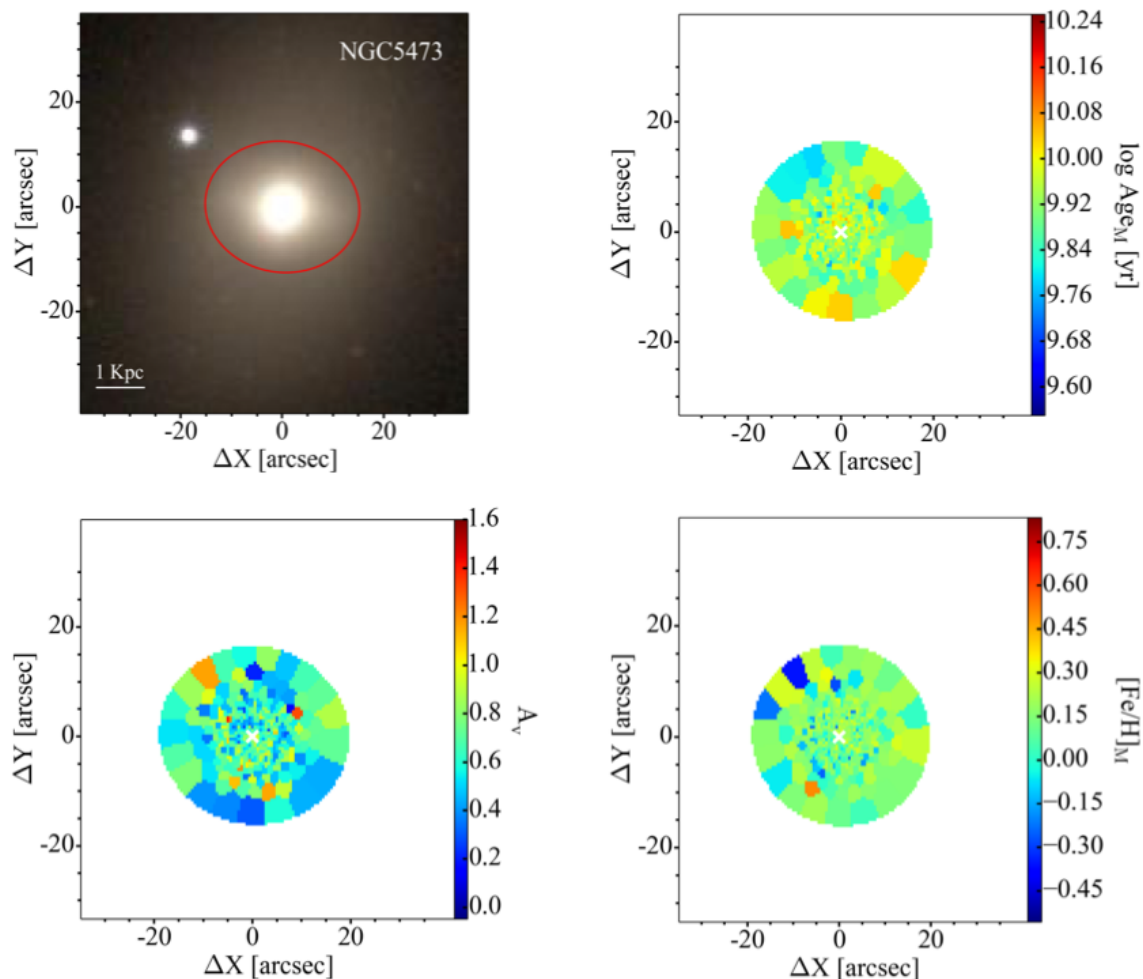


Fig. 22. Illustrative example of the 2D methodology. The top left panel shows a J-PLUS colored composite image of the galaxy NGC5473. The red ellipse delimits a ellipse with the semi-major axis $R = 3 R_{\text{eff}}$. The rest of the panels show the mass-weighted stellar population properties maps ($\log \text{Age}_M$, A_v and $[\text{Fe}/\text{H}]_M$) for this object.

tial new faint members in these clusters, providing a membership probability for each observed source (see Molino et al. 2018, and its Fig. 9 therein for further details). This approach is reassured by the good agreement found between our PDFs and the spectroscopic redshifts for those galaxies for which spectra are available in the literature. This indiscriminate, high quality, photo- z estimation for galaxies in the cluster fields opens the way to statistical studies of cluster membership, while providing valuable data for optimal target selection in spectroscopic follow-ups. In particular, photo- z s produced by J-PLUS are going to be used by the WEAVE cluster surveys in the process of target selection. It is expected that J-PLUS photo- z s will increase the number of selected cluster galaxy members by a factor 2–3. This improvement is particularly relevant in the range of faint magnitudes and in the outskirts of galaxy clusters.

J-PLUS is also suitable to study the intracluster light (ICL), generally defined as the luminous component of galaxy clusters belonging to stars that are gravitationally bound to the cluster gravitational potential, but not locked in any of the individual member galaxies. They are believed to be released through dynamical stripping of stars during the hierarchical process of cluster assembly and growth (Contini et al. 2014). The ICL fraction

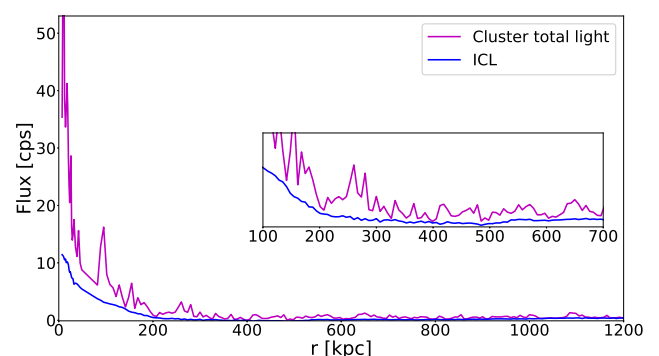


Fig. 23. Radial profiles of the cluster total light (red), and the ICL (blue) in the $J0410$ band.

and its properties are thus key to understand the formation history of galaxy clusters (e.g. Feldmeier et al. 2004; Rudick et al. 2011; Montes & Trujillo 2014), as well as to determine the correct baryon fraction to be compared to cosmological estimates (e.g., Lin & Mohr 2004).

Methods employed in the literature are based on binding energy, local density or surface brightness cut offs. These techniques yield different results in the ICL fraction, with discrepancies up to a factor of four using the same data (Rudick et al. 2011). For this reason, we have developed a method to measure ICL fraction (defined as the ratio between the ICL flux and the total light of the cluster), which is free from *a priori* assumptions of surface brightness profiles and cutoffs (Jiménez-Teja & Dupke 2016). The method is called CICLE (CHEFs ICL Estimator), where the Chebyshev-Fourier functions (CHEFs, Jiménez-Teja & Benítez 2012) are a set of very efficient and compact orthonormal mathematical bases that are able to model galaxies of any morphological type. The CHEFs are used in CICLE to model and remove the light from the galaxies in the field, including the brightest cluster galaxy (BCG). The special configuration of the J-PLUS filter system and the large contiguous area covered by the survey makes it possible to study for the first time the ICL colors of nearby clusters using narrow bands. This yields low resolution information on the spectral energy distribution of the ICL, and provides key information about the origin of this stellar component. As a first example, we show the preliminary results of CICLE implemented on J-PLUS J0410 observations of the Coma cluster, obtaining the profiles shown in Fig. 23 for the ICL and the total luminosity of the cluster. We find a final ICL fraction of 24 % for a radius of ≈ 490 kpc. This is in agreement with previous works and simulations on Coma (Melnick et al. 1977; Bernstein et al. 1995; Adami et al. 2005). Further details are to be found in Jiménez-Teja et al. (in preparation).

4.3. Redshift windows in the distant Universe

The filter set configuration of J-PLUS, including several narrow band filters, allows for a unique search of high redshift targets displaying emission lines. The wide area coverage of the survey compensates its shallow magnitude limit, thus opening a window to explore the abundance and properties of statistical samples of bright ELGs at different redshifts. Many redshift windows provided by the narrow band filters can be used to target a strong optical emission line. Most notably, i) $z \sim 0.77$, when the [O II] $\lambda\lambda 3726, 3729$ doublet enters the J0660 filter; ii) $z \approx 2.1$ (2.2), when the Ly α line enters the J0378 (J0395) filter, and iii) $z \sim 4.4$, when Ly α line enters the J0660 filter.

To identify an emitter and measure its line flux it is necessary to detect a magnitude excess in the narrow-band filter with respect to the adjacent filters that trace the continuum around the line. In the J-PLUS filter configuration, the continuum around a line can be estimated using a combination of the J-PLUS broadband filters. Vilella-Rojo et al. (2015) developed a simple, yet robust methodology to extract the H α flux from local star-forming galaxies using either a combination of three J-PLUS filters (two broad bands and one narrow band), or all the filters via SED fitting (see Sect. 4.2.2 and Logroño-García et al. 2018). These methods can be adapted to other lines at other redshifts.

Typical searches for ELGs using narrow bands are significantly affected by interlopers, i.e., line confusion. With J-PLUS data, all the twelve filters can be used to gain color information that mitigate the impact of emitters at undesired redshifts.

4.3.1. [OII] emission at $z = 0.77$

ELGs at $z \sim 0.77$ are currently being targeted by several ongoing and planned Multi-object spectroscopic (MOS) cosmological surveys, such as 4MOST, DESI, PFS and eBOSS (de Jong

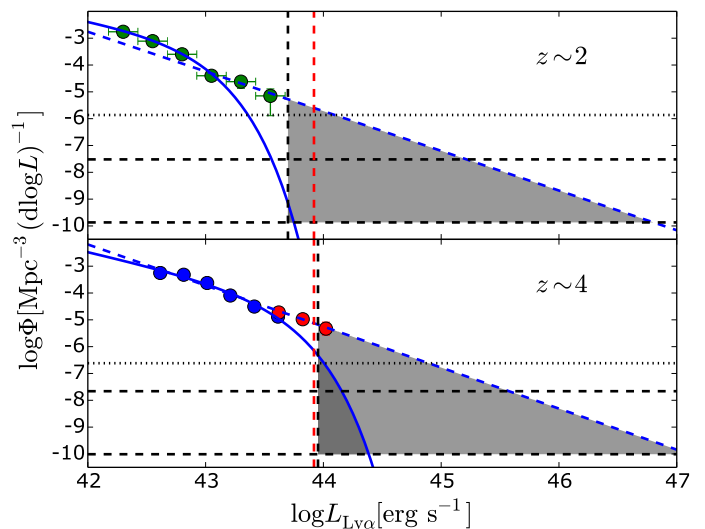


Fig. 24. The bright-end of the LAE luminosity function (LF) accessible by J-PLUS. The gray shaded areas in both panels show the region of the LF that can be probed with the J-PLUS area and flux depth (dark grey for a Schechter-like LF, light gray for a power-law LF). The horizontal dotted/dashed lines represent the lowest possible value of the LF achievable with the J-PLUS EDR/full survey. The black vertical dashed line shows the limiting luminosity of J-PLUS at redshifts 2.2 (*top*) and 4.4 (*bottom*). The vertical red dashed line shows the luminosity of CR7 at $z = 6.604$ (Sobral et al. 2015) for illustration. Green circles in the top panel show the Ly α LF from Sobral et al. (2017). Blue and red circles correspond to the UDS+COSMOS and SA22 samples from Matthee et al. (2015). The solid blue and dashed lines correspond to Schechter and power-law fits to the data, respectively.

et al. 2012; Weinberg et al. 2013; Takada et al. 2014; Delubac et al. 2017). Broad-band target selection designed to select ELGs at $z \sim 0.77$ can deliver success rates of the order of 70 % due to the completeness and purity of the broad band photometry used to define their targets (Raichoor et al. 2017). Since J-PLUS is a photometric survey, its selection function depends only on the depth of the images and the ability to assign the correct redshift to an object with flux excess in a narrow band filter. Thus, the characterization of the ELG population with J-PLUS data is expected to be highly complementary to that coming from MOS facilities.

Assuming a minimum observed equivalent width $EW = 100 \text{ \AA}$, we estimate that we can reach the [O II] line emission down to the luminosity of $\sim 1 \times 10^{42} \text{ erg s}^{-1}$. These objects will be used to characterize the abundance and clustering properties of star-forming galaxies at $z = 0.77$ (Orsi et al., in prep.)

4.3.2. Ly α emission at $z = 2.2$ and 4.4

At higher redshifts, detections are strongly limited by the survey depth. Star-forming Ly α emitting galaxies (Ly α emitters, or LAEs in short) at $z \sim 2$ are expected to be detected down to Ly α luminosities of $\sim 5 \times 10^{43} \text{ erg s}^{-1}$ assuming a minimum observed EW of 100 \AA . At $z = 4.4$, we expect to detect LAEs down to $\sim 9 \times 10^{43} \text{ erg s}^{-1}$.

Sobral et al. (2015) have confirmed spectroscopically an extremely luminous LAE at $z = 6.604$, named CR7, with Ly α luminosity of $8.3 \times 10^{43} \text{ erg s}^{-1}$. A thorough census of these extreme objects has not been yet possible due to the prohibitively large volume required. The J-PLUS dataset can thus perform an unprecedented search for these extremely bright emitters

at high redshifts (Fig. 24). Furthermore, J-PLUS is also expected to detect Ly α blobs (LABs) among the usual high- z , star-forming, Ly α emitting, compact galaxies. LABs are an extremely rare class of Ly α emitters (comoving number density $n_c < 10^{-6} \text{ Mpc}^{-4}$) showing spatially extended Ly α emission ($\sim 30 - 200 \text{ kpc}$ in size, see e.g., Smailagić et al. 2016).

One straightforward approach to select LAE candidates is the three-filter method of Vilella-Rojo et al. (2015) over the filter sets $[u, J0378, g]$ and $[u, J0395, r]$. This method, combined with a selection criteria to assess the narrow-band excess significance (see, e.g., Guaita et al. 2010; Konno et al. 2016), allows to easily extract LAE candidates within J-PLUS EDR (Spinoso et al., in prep.). However, the emission in a single J-PLUS narrow-band is not sufficient to distinguish among the different sources of Ly α emission (star forming galaxies and quasars), as well as to reject interlopers at other redshifts. Quasars constitute a large fraction of the LAE population detectable at the depth of J-PLUS (Fig. 25). While a significant number of $z \sim 2$ quasars has already been observed within SDSS spectroscopic programs, we expect to be able to identify candidate quasars missed by automatized spectroscopic target selection provided that we simply select candidates based on their Ly α emission. This may turn out to be particularly relevant for quasars in the range of magnitudes $r = 12-15$, where SDSS stellar images are usually saturated and J-PLUS photometry can play a unique role.

By exploiting the complete J-PLUS filter set, interlopers at undesired redshifts can be identified by the presence of additional narrow-band excesses other than the one in J0378 or J0395, and removed. This method relies on the assumption that compact star-forming Ly α emitting galaxies at $z \sim 2$ should only exhibit strong line emission at Ly α wavelengths. Our preliminary study also indicates that some combinations of J-PLUS broad-band colours are useful in removing the low- z contaminants. Finally, an additional way to reduce the contamination from line emitters at $z < 2$ is to cross-match the J-PLUS candidates with other public available catalogues. Assuming that high- z LAEs should not exhibit strong emission below the Lyman break, all the sources with a counterpart in the GALEX catalogue can be excluded from our selection. Other undesired contaminants can be removed by cross-matching J-PLUS sources with the SDSS spectroscopically-identified samples of stars and low- z galaxies.

In summary, the J-PLUS filter configuration allows to select samples of emission-line galaxies and quasars in narrow redshift ranges when the line emission can be isolated and characterized. From a preliminary analysis of the J-PLUS EDR, for example, we selected a sample of ~ 30 LAE candidates consistent with $z \approx 2$ Ly α emitting sources, including galaxies and QSOs, which we plan to carefully analyze with spectroscopic follow-up.

4.4. Variable sources

Exposures on each J-PLUS filter are done sequentially, and this provides sensitivity to source variability (either in flux and/or sky position) on time scales shorter than ~ 1 hour. This time scale corresponds to the typical time interval between the first and the last exposure of the same pointing, taking into account all the filters. A clear example for the position variability of a minor body in our solar system can be found in Fig. 26. J-PLUS will hence trace objects that vary their position, such as Solar System minor bodies (Sect. 4.4.1), and their flux, such as cataclysmic variables (Sect. 4.4.2) and variable RR Lyrae stars (Sect. 4.4.3).

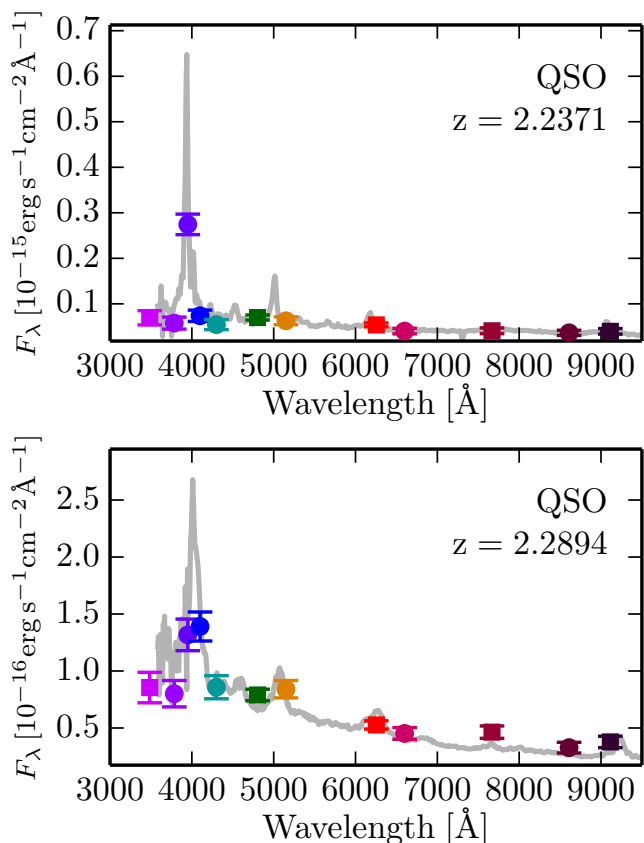


Fig. 25. J-PLUS photo-spectrum of two QSOs with SDSS spectra (marked in Fig. 7), located at $\alpha = 110.11167$, $\delta = 40.23105$, $z = 2.2371$ (top panel), and $\alpha = 110.22740$, $\delta = 40.14428$, $z = 2.2894$ (bottom panel). The Ly α broad-line emission is clear in both sources and is captured by the J0410 filter, showing a relative excess with respect to the continuum traced by both broad-bands and rightmost narrow-band filters.

4.4.1. Minor bodies of the Solar System

All sky photometric surveys like J-PLUS will necessarily observe a large number of minor bodies of the Solar System during normal operation. The majority of the known minor bodies are found in the Main Asteroid Belt, with their orbits confined between Mars' and Jupiter's. Their compositions have a direct relation to the region of the protoplanetary disk where they formed. Bodies that were formed beyond the snow line - the distance from the proto-sun beyond which water ice is stable - would have accreted a considerable amount of ice-rich dust.

The presence of hydrated material in the Main Asteroid Belt has been inferred through the analysis of their reflectance spectra and colours thanks to the presence in the visible spectra of the asteroids of a broad, shallow phyllosilicate band centered around $0.7 \mu\text{m}$. The presence of this band indicates not only that the material were originally rich in water ice, but also that the interior of the body reached temperatures capable of sustaining the presence of liquid water for an extended period of time. The occurrence of this band in asteroids has been mapped using low dispersion spectroscopy, showing that the fraction of asteroids where these bands are observed varies with heliocentric distance, with lower limits of 10% of the observed asteroids at 2.3 AU. This percentage increases to 25% at 3.1 AU and falls towards the outer edge of the Main Asteroid Belt (Carvano et al. 2003).

However, all these data are based on the relatively small sample of asteroids with spectroscopic observations. Although

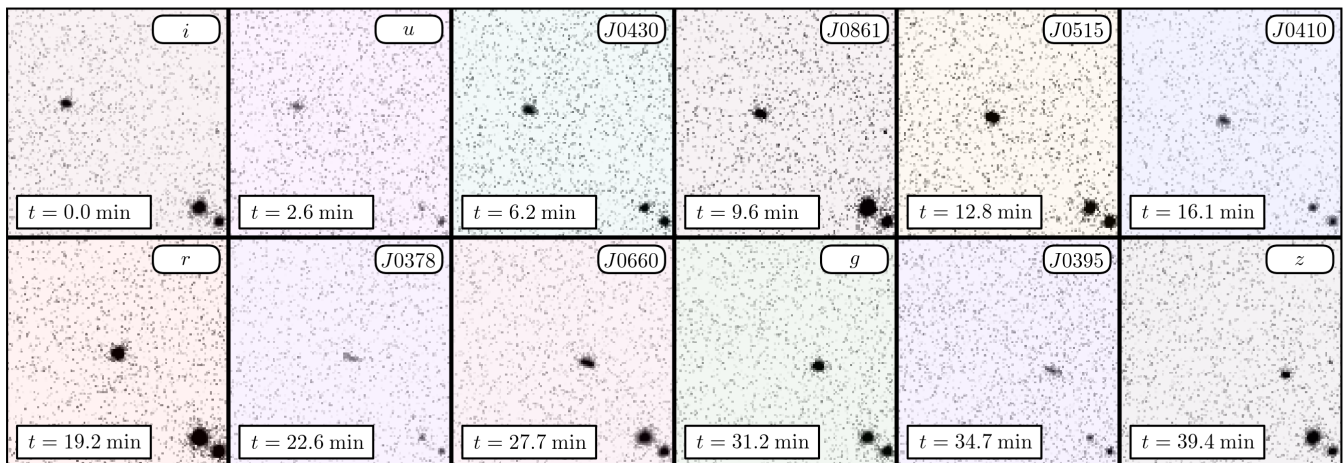


Fig. 26. The 12 J-PLUS band images of the minor body marked in Fig. 7. The observing sequence spans 39.4 min, starting with the *i* band and finishing with the *z* band.

most asteroid taxonomical classes can be defined using intermediate band filters like the SDSS filter system (Carvano et al. 2010), the low spectral resolution tends to render the detection of the $0.7\mu\text{m}$ band unreliable using SDSS data (Rivkin 2012). In this regard, the larger spectral resolution provided by the J-PLUS filter system can provide a better definition of this band, since with J-PLUS the spectral interval covered by the band is sampled also by 2 narrow band filters in addition to the *r*, *i*, and *z* filters. This can be seen on the reflectance spectrum of the asteroid (1024) Hale, obtained from observations taken during normal survey conditions, see Fig. 27.

One way to compare and quantify the sensitivity of the SDSS and J-PLUS filter systems to the $0.7\mu\text{m}$ band is to use low resolution spectra of asteroids with this feature as templates to produce synthetic reflectances for each filter. We use 5 spectra of asteroids from the hydrated asteroid family of Erigone to produce a sample of 1000 synthetic spectra with Gaussian random uncertainties in reflectance driven around the nominal reflectance values and with nominal RMS. A similar set of clones were generated using a synthetic flat spectra to simulate a non-hydrated asteroid. To define whether each clone had a band or not, we generate further 1000 instances of the measurements by again randomly sampling reflectances normally distributed around each reflectance measured value. We next measure, for each realization, the parameter associated to the presence of the band. The distribution of the parameters are then compared using a Kolmogorov-Smirnov (K-S) test to the distribution obtained from featureless reference spectra with the same uncertainties. We accept the band as real if the K-S test indicates that the distributions are statistically different and if the parameter associated with the band presence is larger than a given threshold. This exercise is performed using the SDSS and J-PLUS filter systems. For the SDSS, the parameter associated with the presence of the band is the reflectance at *i* on the spectra normalized by the gradient of reflectance between *g* and *z* (with values above that continua set as negative). For J-PLUS this parameter is the sum of area of the polygon formed by the segment that connects the *r*, J0660, *i*, J0861, and *z* bands, and the continuum defined by the segment between the *r* and *z* filters, with areas above that line counted as negative. Figure 28 shows the fraction of clones in which band detection occurred among the samples corresponding to templates with (solid lines) and without the feature (dashed lines), using the SDSS and the J-PLUS filter sets, as

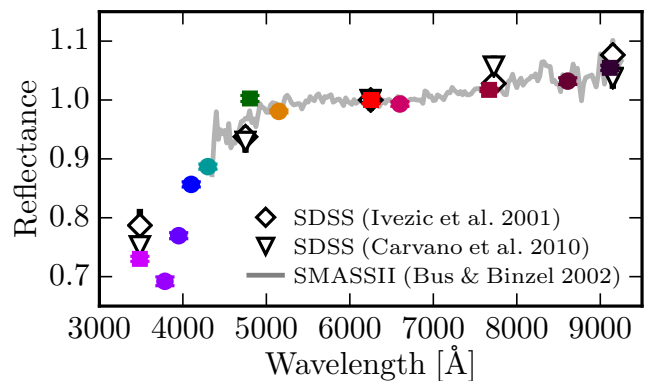


Fig. 27. Reflectance spectrum of the hydrated asteroid (1024) Hale obtained from J-PLUS observations, together with two sets of reflectance spectra from SDSS observations (Ivezić et al. 2001; Carvano et al. 2010) and other obtained with low dispersion spectroscopy (Bus & Binzel 2002). All spectra normalized at the *r* band. The J-PLUS observations were made during normal survey operation on 2017-01-07 while the asteroid had $V = 15.2$ mag. The solar colours used to obtain the J-PLUS reflectance spectrum were calculated using a reference solar spectrum from Chance & Kurucz (2010). The resulting error bars are smaller than the size of the points in the figure.

a function of the assumed uncertainty of the reflectances. This result shows that the J-PLUS filter set is more effective in detecting the band than the SDSS filter set. In particular, the results obtained with the J-PLUS filter set present a considerable smaller number of false positive in comparison with data obtained with the SDSS filters, with the difference as high as $\sim 29\%$ less false detections for 1% uncertainties in the reflectances.

Using data from the observations obtained so far it is possible to estimate the depth at which asteroids can be expected to be observed during the survey. We find that the detection efficiency at the bluer filters starts to fall around $V = 17.5$ mag, but for the filters involved in the detection of the $0.7\mu\text{m}$ band the detection efficiency remains high up to $V = 19$ mag. Simulations indicate that during the survey execution time over ten thousands known asteroids brighter than $V = 19$ mag will be observed. Therefore, once completed the J-PLUS data set of minor bodies will provide a valuable tool to probe the distribution of hydration in the Main Asteroid Belt.

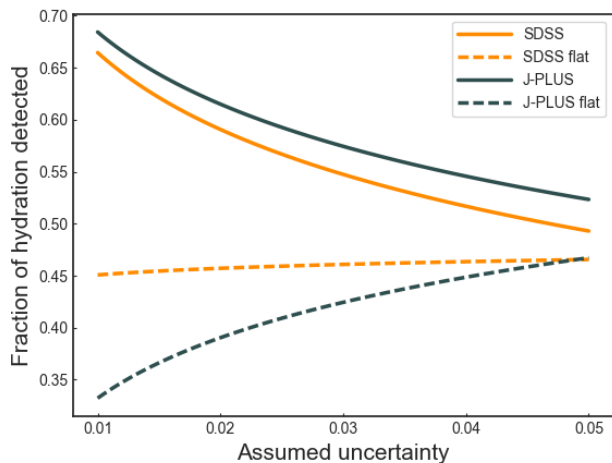


Fig. 28. Fraction of clones where the algorithm reported the presence of a band using SDSS and J-PLUS filters as a function of the assumed uncertainty of the reflectances. The curves corresponding to hydrated template spectra are drawn with solid lines, while those corresponding to flat spectra templates are given by the dashed lines.

4.4.2. Searching for Cataclysmic Variables

Cataclysmic variables (CVs) are interacting binary stars made of a white dwarf and a main sequence star which is losing mass through Roche lobe overflow (for a review, see Warner 1995). Historically, CVs have been discovered through their variability properties and, most recently, as by-products of quasar searches (for a review, see Gänsicke 2005). In fact, SDSS discovered more than 400 new CVs (Szkody et al. 2011). Depending on the mass transfer rate, the magnetic activity of the white dwarf and the inclination of the system CVs can display a variety of observational properties. Therefore, in general terms, a CV spectrum can be blue and/or red and due to the accretion disk it uses to show H_α emission. We checked that from all the CVs of the catalogue by Ritter & Kolb (2003) only one (J0743+4106) falls within the EDR footprint (shown in Fig. 29). The SED clearly shows the blue and red appearance due to the two stars of the binary as well as the H_α emission of the accretion disc. Interestingly, the SDSS spectrum looks completely different, being clearly dominated by the continuum of the disc (as would be expected in a high mass-accretion phase). In Abril et al. (in prep.), we propose a new methodology, based on the J-PLUS filter set, which can be used to separate CVs from other type of astrophysical sources, in particular quasars. Our expectations are that J-PLUS will detect around 4 000 CVs.

4.4.3. RR Lyrae stars

RR Lyrae stars are evolved low mass stars burning He in their core that can be found in a region of the Hertzsprung–Russel Diagram where the Horizontal Branch (HB) crosses the instability strip. These type of stars undergo radial oscillations and they are classified according to the excited oscillation mode they suffer: fundamental mode oscillators only (RRab type), first overtone

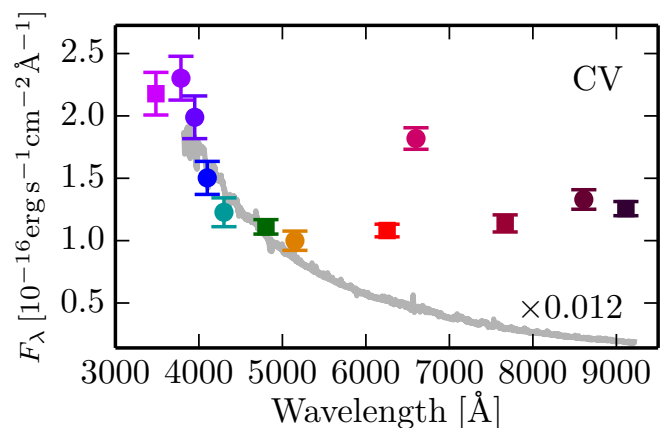


Fig. 29. J-PLUS photo-spectrum of the cataclysmic variable J0743+4106. The blue side of the spectrum is dominated by the white dwarf emission while the red side is dominated by the secondary star. The $J0660$ filter shows the prominent H_α emission of the disc. For comparison, the spectrum from SDSS DR12 is shown in gray (but multiplied by a factor 0.012 to match the bluest filters). This spectrum was clearly obtained during a high mass-accretion phase while the J-PLUS photometry was obtained during a low mass-accretion phase.

oscillators (RRc) or fundamental and first overtone oscillators (RRd).

The large and indiscriminate area J-PLUS will observe, together with the survey’s depth, makes it very convenient for deriving properties of the Galactic halo structure. Among the stars than can be used for that purpose, RR Lyrae stars are of outstanding importance for several reasons: i) they are ubiquitous species in our Galaxy, so they can be found distributed virtually everywhere without being linked to any particular Galactic component; ii) they are relatively bright ($M_V \approx 0.6$ for mean halo metallicity), so they are easily detectable up to a few hundred kpc from us; iii) their pulsation periods obey a period-luminosity-metallicity relation that makes them standard candles, becoming very useful to constraint distances; iv) they are relatively old stars, so they are fair tracers of the MW old component. For all these reasons RR Lyrae stars are excellent tracers of the structure of the Galactic halo (e.g. Sarajedini 2011).

On the observational side, their pulsation amplitude (from 0.2 to 1.5 magnitudes) and period (from 5 h to 1.2 days) make their variability relatively easy to be detected using both, J-PLUS and external data archives. Additionally, J-PLUS will provide the SED of a unprecedented amount of RR Lyrae stars. Two examples are shown in Fig. 30, taken from the J-PLUS EDR.

5. Summary and conclusions

This paper is devoted to present and illustrate the J-PLUS survey and its main scientific applications. J-PLUS is a 12-band photometric survey of thousands of square degrees in the Northern hemisphere which is being conducted at the OAJ. The most remarkable characteristics of the survey rely on the 2 deg^2 FoV of T80Cam at the JAST/T80 telescope and on a unique system of 12 optical filters, including broad band, medium width, and narrow band optical filters in the range 3 500–10 000 Å. This filter system has been designed to optimally extract rest-frame spectral features that are key to characterize the stellar types in our MW as well as to perform stellar population and star formation studies in nearby galaxies. Overall, J-PLUS provides an

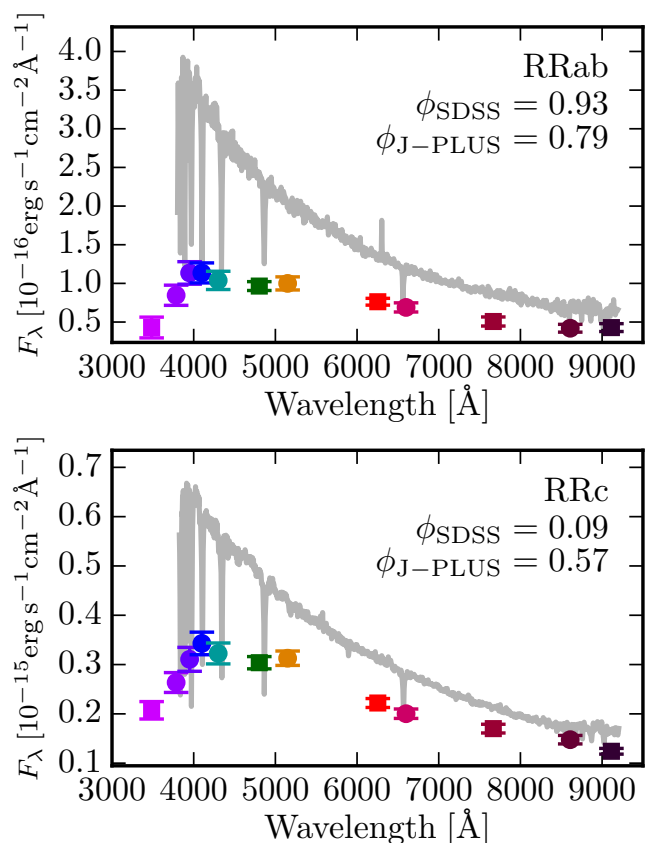


Fig. 30. J-PLUS photo-spectra of two RR Lyrae stars, one type RRab (top panel; $\alpha = 122.9568$ deg, $\delta = 31.089$ deg) and one type RRc (bottom panel; $\alpha = 123.6246$ deg, $\delta = 31.188$ deg). The gray lines show the SDSS spectra of these stars. The J-PLUS photo-spectra and the SDSS spectra were acquired at different pulsation phases ϕ , as labeled in the panels, with $\phi = 0, 1$ corresponding to the maximum flux of the source (i.e., the entire period is covered by the ϕ range of values $\phi \in [0, 1)$). Both SDSS spectra were taken not far from their respective maximum brightnesses.

unprecedented low resolution photo-spectrum of 12 points for every pixel of the sky in the footprint of the survey.

The paper is also aimed to release the first 36 deg^2 of J-PLUS data, amounting to $\sim 1.5 \times 10^5$ stars and 10^5 galaxies at $r < 21$ mag observed in 12 broad, intermediate and narrow optical bands. This dataset is used to illustrate some of the science cases that will be addressed by J-PLUS. As of early 2018, J-PLUS has already mapped more than $1\,000 \text{ deg}^2$, providing unprecedented information of the SED for millions of stars and galaxies. A forthcoming data release with a significantly larger area to the one presented in this paper is expected to be published along 2018.

With a choice of narrow and medium width filters strategically placed to render accurate stellar type information (the $3\,700\text{--}4\,000 \text{ \AA}$ Balmer break region, $H\delta$, Ca H+K, the G-band, the Mgb and Ca triplets), the addition of narrow band filters centred upon the $H\alpha/\lambda 6563$ and $[OII]/\lambda 3727$ lines constitutes a powerful window to the star formation activity in the local universe, and also to bright emission lines at higher redshifts. Consequently, J-PLUS is providing a unique data set with direct applications in the characterization of the stellar populations of our Galaxy, including metal poor stars, white dwarfs, ultracool dwarfs, planetary nebulae, symbiotic stars, cataclysmic variables, and globular clusters. The same set of filters enable IFU-like 2D

studies in nearby ($z < 0.015$) galaxies with unprecedented quality and statistics, and provides high-quality photo- z estimates (with an error amplitude of $\delta z \sim 0.01\text{--}0.03$ for $r < 21$ mag) for extragalactic objects. In addition, in the extragalactic sky, J-PLUS' narrow band filters provide sensitivity to particular redshift shells in the universe corresponding to the rest-frame frequency of power lines like $\text{Ly}\alpha$ or $[OII]/\lambda 3727$.

A great part of the added value of J-PLUS resides, besides its large scale/panoramic character owed to its 2 deg^2 FoV, in the medium-width and narrow band filters. These bring J-PLUS along the way of other spectro-photometric surveys where multiple band imaging is used as an alternative to spectroscopy. The indiscriminate nature of this approach, which drastically simplifies selection biases, together with the significantly larger statistics of the resulting catalogues, constitute two powerful arguments supporting this strategy. While the upcoming J-PAS project can be seen as the definite test where all these expectations will be confronted with real data, J-PLUS is currently paving exactly the same way but under more modest instrumentation. Nonetheless, despite the intrinsic scientific interest of J-PLUS, it turns out to be an ideal, strategical test bench for J-PAS as most technical and software developments of J-PLUS will apply very similarly to J-PAS. In addition, all these efforts are being complemented by the twin project S-PLUS, which, from Cerro Tololo, is scanning the Southern hemisphere with a replica of the J-PLUS telescope, camera and filter system.

The combination of this type of surveys with spectroscopic ones for calibration and comparison purposes, and from other surveys at other wavelength ranges such as X-ray or γ -ray, should significantly improve our knowledge of the SEDs for practically *all* families of sources in our universe. Furthermore, if systematics are kept under the required level, this spectro-photometric approach should also open the possibility to study the unresolved emission associated to particular emission lines at particular redshift shells (aka intensity mapping, Kovetz et al. 2017), thus providing a new way to conduct tomography of the universe in the optical range.

To conclude, J-PLUS may thus be opening an exciting and interesting new phase in optical, large scale, astrophysical surveys. Ultimately, J-PLUS will become a powerful multicolor view of the nearby Universe that will observe and characterize tens of millions of galaxies and stars of the MW halo, with a wide range of astrophysical applications and a striking potential for bringing unexpected discoveries to our knowledge of the Universe. The J-PLUS data will be made public progressively in subsequent data releases, an expression of its commitment to become a major legacy project for the astronomy and astrophysics of the next decades.

Acknowledgements. Funding for the J-PLUS Project has been provided by the Governments of Spain and Aragón through the Fondo de Inversiones de Teruel, the Spanish Ministry of Economy and Competitiveness (MINECO; under grants AYA2017-86274-P, AYA2016-77846-P, AYA2016-77237-C3-1-P, AYA2015-66211-C2-1-P, AYA2015-66211-C2-2, AYA2012-30789, AGAUR grant SGR-661/2017, and ICTS-2009-14), and European FEDER funding (FCDD10-4E-867, FCDD13-4E-2685). Further support has been provided by the Ramón y Cajal programmes RYC-2016-20254, RYC-2011-08262 and RYC-2011-08529. This research has made use of the Spanish Virtual Observatory (<http://svo.cab.inta-csic.es>) supported from the Spanish MINECO through grant AYA2014-55216. We also acknowledge Spanish CSIC (I-COOP+ 2016 program) through grant COOPB20263. The Brazilian agencies FAPESP and the National Observatory of Brazil have also contributed to this project. We acknowledge financial support from the Fundação Carlos Chagas Filho de Amparo à Pesquisa do Estado do Rio de Janeiro - FAPERJ (fellowship Nota 10, PDR-10), from CNPq through BP grant 312307/2015-2 and Universal Grants 459553/2014-3, PQ 302037/2015-2, and PDE 200289/2017-9), FINEP grants REF. 1217/13 - 01.13.0279.00 and REF 0859/10 - 01.10.0663.00, from FAPERJ grant E-26/202.835/2016, and CAPES (Science without Bor-

ders program, Young Talent Fellowship, BJT) through grants A062/2013 and CAPES-PNPD 2940/2011. The FAPESP grants no. 2015/12745-6, 2014/11338-5, 2014/07684-5, 2013/04582-4 and 2009/54202-8 are also acknowledged. Finally, the authors acknowledge partial support from grant PHY 14-30152; Physics Frontier Center/JINA Center for the Evolution of the Elements (JINACEE), awarded by the US National Science Foundation.

References

- Adami, C., Slezak, E., Durret, F., et al. 2005, *A&A*, 429, 39
- Allende Prieto, C. 2016, *A&A*, 595, A129
- Allende Prieto, C., Beers, T. C., Wilhelm, R., et al. 2006, *ApJ*, 636, 804
- Allende Prieto, C., K. L. H. I. B. M. A. B. P. S. & Nahar, S. N. 2018, *A&A*
- An, D., Beers, T. C., Santucci, R. M., et al. 2015, *ApJ*, 813, L28
- Bailer-Jones, C. A. L. 2004, *A&A*, 419, 385
- Bastian, N. 2015, ArXiv e-prints
- Baum, W. A. 1962, in *IAU Symposium*, Vol. 15, Problems of Extra-Galactic Research, ed. G. C. McVittie, 390
- Bayo, A., Rodrigo, C., Barrado Y Navascués, D., et al. 2008, *A&A*, 492, 277
- Beers, T. C. & Christlieb, N. 2005, *ARA&A*, 43, 531
- Benitez, N., Dupke, R., Moles, M., et al. 2014a, ArXiv e-prints
- Benitez, N., Dupke, R., Moles, M., et al. 2014b, ArXiv e-prints
- Benítez, N., Moles, M., Aguerri, J. A. L., et al. 2009, *ApJ*, 692, L5
- Bernstein, G. M., Nichol, R. C., Tyson, J. A., Ulmer, M. P., & Wittman, D. 1995, *AJ*, 110, 1507
- Bertin, E. 2006, in *Astronomical Society of the Pacific Conference Series*, Vol. 351, *Astronomical Data Analysis Software and Systems XV*, ed. C. Gabriel, C. Arviset, D. Ponz, & S. Enrique, 112
- Bertin, E. & Arnouts, S. 1996, *A&AS*, 117, 393
- Bertin, E., Mellier, Y., Radovich, M., et al. 2002, in *Astronomical Society of the Pacific Conference Series*, Vol. 281, *Astronomical Data Analysis Software and Systems XI*, ed. D. A. Bohlender, D. Durand, & T. H. Handley, 228
- Boender, C., K. A. R. T. A. & Stougie, L. 1982, *Mathematical Programming*, 22, 125
- Bonatto, C., Chies-Santos, A. L., Coelho, P. R. T., & J-PLUS collaboration. 2018, *A&A*, submitted
- Bonnarel, F., Fernique, P., Bienaymé, O., et al. 2000, *A&AS*, 143, 33
- Bundy, K., Bershad, M. A., Law, D. R., et al. 2015, *ApJ*, 798, 7
- Bus, S. J. & Binzel, R. P. 2002, *Icarus*, 158, 106
- Cappellari, M., Emsellem, E., Krajnović, D., et al. 2011, *MNRAS*, 413, 813
- Cardamone, C. N., van Dokkum, P. G., Urry, C. M., et al. 2010, *ApJS*, 189, 270
- Carretta, E., Bragaglia, A., Gratton, R., D’Orazi, V., & Lucatello, S. 2009, *A&A*, 508, 695
- Carvano, J. M., Hasselmann, P. H., Lazzaro, D., & Mothé-Diniz, T. 2010, *A&A*, 510, A43
- Carvano, J. M., Mothé-Diniz, T., & Lazzaro, D. 2003, *Icarus*, 161, 356
- Cenarro, A. J., Cardiel, N., Gorgas, J., et al. 2001a, *MNRAS*, 326, 959
- Cenarro, A. J., Cardiel, N., Vazdekis, A., & Gorgas, J. 2009, *MNRAS*, 396, 1895
- Cenarro, A. J., Moles, M., Cristóbal-Hornillos, D., et al. 2010, in *Society of Photo-Optical Instrumentation Engineers (SPIE) Conference Series*, Vol. 7738, *Society of Photo-Optical Instrumentation Engineers (SPIE) Conference Series*, 0
- Cenarro, A. J., Moles, M., Cristóbal-Hornillos, D., et al. 2012, in *Society of Photo-Optical Instrumentation Engineers (SPIE) Conference Series*, Vol. 8448, *Society of Photo-Optical Instrumentation Engineers (SPIE) Conference Series*
- Cenarro, A. J., Moles, M., Marín-Franch, A., et al. 2014, in *Society of Photo-Optical Instrumentation Engineers (SPIE) Conference Series*, Vol. 9149, *Society of Photo-Optical Instrumentation Engineers (SPIE) Conference Series*
- Chance, K. & Kurucz, R. L. 2010, *J. Quant. Spec. Radiat. Transf.*, 111, 1289
- Chueca, S., Marín-Franch, A., Cenarro, A. J., et al. 2012, in *Society of Photo-Optical Instrumentation Engineers (SPIE) Conference Series*, Vol. 8450, *Society of Photo-Optical Instrumentation Engineers (SPIE) Conference Series*
- Ciardullo, R. 2012, *Ap&SS*, 341, 151
- Contini, E., De Lucia, G., Villalobos, Á., & Borgani, S. 2014, *MNRAS*, 437, 3787
- Covey, K. R., Ivezić, Ž., Schlegel, D., et al. 2007, *AJ*, 134, 2398
- Cristóbal-Hornillos, D., Varela, J., Ederoclite, A., et al. 2014, in *Proc. SPIE*, Vol. 9152, *Software and Cyberinfrastructure for Astronomy III*, 91520O
- Croom, S. M., Lawrence, J. S., Bland-Hawthorn, J., et al. 2012, *MNRAS*, 421, 872
- de Jong, R. S., Bellido-Tirado, O., Chiappini, C., et al. 2012, in *Proc. SPIE*, Vol. 8446, *Ground-based and Airborne Instrumentation for Astronomy IV*, 84460T
- de Zeeuw, P. T., Bureau, M., Emsellem, E., et al. 2002, *MNRAS*, 329, 513
- Delubac, T., Raichoor, A., Comparat, J., et al. 2017, *MNRAS*, 465, 1831
- Di Stefano, R. 2010, *ApJ*, 719, 474
- Díaz-García, L. A., Cenarro, A. J., López-Sanjuan, C., et al. 2015, *A&A*, 582, A14
- Dilday, B., Howell, D. A., Cenko, S. B., et al. 2012, *Science*, 337, 942
- Drew, J. E., Gonzalez-Solares, E., Greimel, R., et al. 2014, *MNRAS*, 440, 2036
- Drew, J. E., Greimel, R., Irwin, M. J., et al. 2005, *MNRAS*, 362, 753
- Feldmeier, J. J., Mihos, J. C., Morrison, H. L., et al. 2004, *ApJ*, 609, 617
- Ferland, G. J., Porter, R. L., van Hoof, P. A. M., et al. 2013, *Rev. Mexicana Astron. Astrofis.*, 49, 137
- Fukugita, M., Ichikawa, T., Gunn, J. E., et al. 1996, *AJ*, 111, 1748
- Gaia Collaboration, Prusti, T., de Bruijne, J. H. J., et al. 2016, *A&A*, 595, A1
- Gänsicke, B. T. 2005, in *Astronomical Society of the Pacific Conference Series*, Vol. 330, *The Astrophysics of Cataclysmic Variables and Related Objects*, ed. J.-M. Hameury & J.-P. Lasota, 3
- Goddard, D., Thomas, D., Maraston, C., et al. 2017, *MNRAS*, 466, 4731
- Gonçalves, D. R., Magrini, L., de la Rosa, I. G., & Akras, S. 2015, *MNRAS*, 447, 993
- Gonçalves, D. R., Magrini, L., Martins, L. P., Teodorescu, A. M., & Quireza, C. 2012, *MNRAS*, 419, 854
- Gonçalves, D. R., Magrini, L., Munari, U., Corradi, R. L. M., & Costa, R. D. D. 2008, *MNRAS*, 391, L84
- Gratton, R. G., Carretta, E., & Bragaglia, A. 2012, *A&A Rev.*, 20, 50
- Gregg, M. D., Silva, D., Rayner, J., et al. 2006, in *The 2005 HST Calibration Workshop: Hubble After the Transition to Two-Gyro Mode*, ed. A. M. Koekoemoer, P. Goudfrooij, & L. L. Dressel, 209
- Grillmair, C. J. & Dionatos, O. 2006, *ApJ*, 643, L17
- Guaita, L., Gawiser, E., Padilla, N., et al. 2010, *ApJ*, 714, 255
- Harris, W. E. 2010, ArXiv e-prints
- Heap, S. R. & Lindler, D. J. 2007, in *Astronomical Society of the Pacific Conference Series*, Vol. 374, *From Stars to Galaxies: Building the Pieces to Build Up the Universe*, ed. A. Vallenari, R. Tantaló, L. Portinari, & A. Moretti, 409
- Hickson, P., Gibson, B. K., & Callaghan, K. A. S. 1994, *MNRAS*, 267, 911
- High, F. W., Stubbs, C. W., Rest, A., Stalder, B., & Challis, P. 2009, *AJ*, 138, 110
- Ilbert, O., Capak, P., Salvato, M., et al. 2009, *ApJ*, 690, 1236
- Ivezić, Ž., Sesar, B., Jurić, M., et al. 2008, *ApJ*, 684, 287
- Ivezić, Ž., Tabachnik, S., Rafikov, R., et al. 2001, *AJ*, 122, 2749
- Jiménez-Teja, Y. & Benítez, N. 2012, *ApJ*, 745, 150
- Jiménez-Teja, Y. & Dupke, R. 2016, *ApJ*, 820, 49
- Jordi, C., Høg, E., Brown, A. G. A., et al. 2006, *MNRAS*, 367, 290
- Kaiser, N., Aussel, H., Burke, B. E., et al. 2002, in *Proc. SPIE*, Vol. 4836, *Survey and Other Telescope Technologies and Discoveries*, ed. J. A. Tyson & S. Wolff, 154–164
- Kelly, P. L., von der Linden, A., Applegate, D. E., et al. 2014, *MNRAS*, 439, 28
- Kennicutt, Jr., R. C. 1998, *ARA 'I&A*, 36, 189
- Kesseli, A. Y., West, A. A., Veyette, M., et al. 2017, ArXiv e-prints
- Kheirastan, S. & Bazarghan, M. 2016, *Ap&SS*, 361, 304
- Konno, A., Ouchi, M., Nakajima, K., et al. 2016, *ApJ*, 823, 20
- Kovetz, E. D., Viero, M. P., Lidz, A., et al. 2017, ArXiv e-prints
- Kuntschner, H., Emsellem, E., Bacon, R., et al. 2010, *MNRAS*, 408, 97
- Kwitter, K. B. & Henry, R. B. C. 1998, *ApJ*, 493, 247
- Kwitter, K. B., Henry, R. B. C., & Milingo, J. B. 2003, *PASP*, 115, 80
- Larsen, S. S., Baumgardt, H., Bastian, N., et al. 2015, *ApJ*, 804, 71
- Le Borgne, J.-F., Bruzual, G., Pelló, R., et al. 2003, *A&A*, 402, 433
- Lee, Y. S., Beers, T. C., Sivarani, T., et al. 2008, *AJ*, 136, 2022
- Lin, Y.-T. & Mohr, J. J. 2004, *ApJ*, 617, 879
- Logroño-García, R., Vilella-Rojo, G., López-Sanjuan, C., & J-PLUS collaboration. 2018, *A&A*, submitted
- López-Sanjuan, C., Vázquez Ramió, H., Varela, J., & J-PLUS collaboration. 2018, *A&A*, submitted
- Magrini, L., Gonçalves, D. R., & Vajgel, B. 2017, *MNRAS*, 464, 739
- Magrini, L., Stanghellini, L., & Gonçalves, D. R. 2012, in *IAU Symposium*, Vol. 283, *IAU Symposium*, 251–258
- Marín-Franch, A., Chueca, S., Moles, M., et al. 2012, in *Society of Photo-Optical Instrumentation Engineers (SPIE) Conference Series*, Vol. 8450, *Society of Photo-Optical Instrumentation Engineers (SPIE) Conference Series*
- Marín-Franch, A., Taylor, K., Cenarro, J., Cristóbal-Hornillos, D., & Moles, M. 2015, *IAU General Assembly*, 22, 2257381
- Marín-Franch, A., Taylor, K., Cepa, J., et al. 2012, in *Society of Photo-Optical Instrumentation Engineers (SPIE) Conference Series*, Vol. 8446, *Society of Photo-Optical Instrumentation Engineers (SPIE) Conference Series*
- Martí, P., Miquel, R., Castander, F. J., et al. 2014, *MNRAS*, 442, 92
- Mathee, J., Sobral, D., Santos, S., et al. 2015, *MNRAS*, 451, 400
- Melnick, J., Hoessel, J., & White, S. D. M. 1977, *MNRAS*, 180, 207
- Moles, M., Benítez, N., Aguerri, J. A. L., et al. 2008, *AJ*, 136, 1325
- Moles, M., Sánchez, S. F., Lamadrid, J. L., et al. 2010, *PASP*, 122, 363
- Molino, A., Benítez, N., Moles, M., et al. 2014, *MNRAS*, 441, 2891
- Molino, A., Costa-Duarte, M. V., Mendes de Oliveira, C., & J-PLUS collaboration. 2018, *A&A*, submitted
- Montes, M. & Trujillo, I. 2014, *ApJ*, 794, 137
- Mukai, K., Luna, G. J. M., Cusumano, G., et al. 2016, *MNRAS*, 461, L1
- Munari, U. & Zwitter, T. 2002, *A&A*, 383, 188

- Otsuka, M., Hyung, S., & Tajitsu, A. 2015, *ApJS*, 217, 22
- Parker, Q. A., Cohen, M., Stupar, M., et al. 2012, *MNRAS*, 427, 3016
- Pereira, C.-B. & Miranda, L.-F. 2007, *A&A*, 467, 1249
- Pérez-González, P. G., Cava, A., Barro, G., et al. 2013, *ApJ*, 762, 46
- Placco, V. M., Frebel, A., Lee, Y. S., et al. 2015, *ApJ*, 809, 136
- Postman, M., Coe, D., Benítez, N., et al. 2012, *ApJS*, 199, 25
- Raichoor, A., Comparat, J., Delubac, T., et al. 2017, *ArXiv e-prints*
- Richer, M. G., Tovmassian, G., Stasińska, G., et al. 2002, *A&A*, 395, 929
- Ritter, H. & Kolb, U. 2003, *A&A*, 404, 301
- Rivkin, A. S. 2012, *Icarus*, 221, 744
- Rodríguez-Flores, E. R., Corradi, R. L. M., Mampaso, A., et al. 2014, *A&A*, 567, A49
- Rudick, C. S., Mihos, J. C., & McBride, C. K. 2011, *ApJ*, 732, 48
- Salvadori, S., Ferrara, A., Schneider, R., Scannapieco, E., & Kawata, D. 2010, *MNRAS*, 401, L5
- San Roman, I., Cenarro, A. J., Díaz-García, L. A., et al. 2018a, *A&A*, 609, A20
- San Roman, I., Sánchez-Blázquez, P., Cenarro, A. J., & J-PLUS collaboration. 2018b, *A&A*, in prep.
- Sánchez, S. F., Kennicutt, R. C., Gil de Paz, A., et al. 2012, *A&A*, 538, A8
- Sánchez-Blázquez, P., Forbes, D. A., Strader, J., Brodie, J., & Proctor, R. 2007, *MNRAS*, 377, 759
- Sánchez-Blázquez, P., Gorgas, J., & Cardiel, N. 2006, *A&A*, 457, 823
- Sarajedini, A. 2011, in *RR Lyrae Stars, Metal-Poor Stars, and the Galaxy*, ed. A. McWilliam, Vol. 5, 181
- Smailagić, M., Micic, M., & Martinović, N. 2016, *MNRAS*, 459, 84
- Sobral, D., Matthee, J., Best, P., et al. 2017, *MNRAS*, 466, 1242
- Sobral, D., Matthee, J., Darvish, B., et al. 2015, *ApJ*, 808, 139
- Spolaor, M., Kobayashi, C., Forbes, D. A., Couch, W. J., & Hau, G. K. T. 2010, *MNRAS*, 408, 272
- Szkody, P., Anderson, S. F., Brooks, K., et al. 2011, *AJ*, 142, 181
- Takada, M., Ellis, R. S., Chiba, M., et al. 2014, *PASJ*, 66, R1
- van Dokkum, P. G. 2001, *PASP*, 113, 1420
- Varela, J., Cristóbal-Hornillos, D., Cenarro, J., et al. 2014, in *IAU Symposium, Vol. 306, Statistical Challenges in 21st Century Cosmology*, ed. A. Heavens, J.-L. Starck, & A. Krone-Martins, 359–361
- Vickers, J. J., Grebel, E. K., & Huxor, A. P. 2012, *AJ*, 143, 86
- Viironen, K., Greimel, R., Corradi, R. L. M., et al. 2009, *A&A*, 504, 291
- Vilella-Rojo, G., Viironen, K., López-Sanjuan, C., et al. 2015, *A&A*, 580, A47
- Warner, B. 1995, *Cambridge Astrophysics Series*, 28
- Weinberg, D., Bard, D., Dawson, K., et al. 2013, *ArXiv e-prints*
- Wenger, M., Ochsenein, F., Egret, D., et al. 2000, *A&AS*, 143, 9
- West, A. A., Bochanski, J. J., Bowler, B. P., et al. 2011, in *Astronomical Society of the Pacific Conference Series, Vol. 448, 16th Cambridge Workshop on Cool Stars, Stellar Systems, and the Sun*, ed. C. Johns-Krull, M. K. Browning, & A. A. West, 531
- Whelan, J. & Iben, Jr., I. 1973, *ApJ*, 186, 1007
- Wilkinson, D. M., Maraston, C., Thomas, D., et al. 2015, *MNRAS*, 449, 328
- Wolf, C., Meisenheimer, K., Rix, H.-W., et al. 2003, *A&A*, 401, 73
- Xavier, H. S., Abramo, L. R., Sako, M., et al. 2014, *MNRAS*, 444, 2313
- Yanny, B., Rockosi, C., Newberg, H. J., et al. 2009, *AJ*, 137, 4377
- York, D. G., Adelman, J., Anderson, Jr., J. E., et al. 2000, *AJ*, 120, 1579
- ¹¹ Department of Physics and JINA Center for the Evolution of the Elements, University of Notre Dame, Notre Dame, IN 46556, USA
- ¹² Centro de Astrobiología, CSIC-INTA, ESAC campus, camino bajo del castillo s/n, E-28 692 Villanueva de la Cañada, Madrid, Spain
- ¹³ Departamento de Física, Universidade Federal do Rio Grande do Norte, 59072-970 Natal, RN, Brazil
- ¹⁴ Departamento de Física, Universidade Federal de Sergipe (UFS), Av. Marechal Rondon, S/N, 49000-000 São Cristóvão, SE, Brazil
- ¹⁵ X-ray Astrophysics Laboratory, NASA Goddard Space Flight Center, Greenbelt, MD 20771, USA
- ¹⁶ Department of Physics, University of Maryland, Baltimore County, 1000 Hilltop Circle, Baltimore, MD 21250, USA
- ¹⁷ Tartu Observatory, Tartu University, Observatooriumi 1, Tõravere, 61602 Tartu maakond, Estonia
- ¹⁸ Instituto de Física, Universidade de São Paulo, Rua do Matão 1371, 05508-090, São Paulo, SP, Brazil
- ¹⁹ Instituto de Astrofísica de Andalucía (IAA), Consejo Superior de Investigaciones Científicas (CSIC), Glorieta de Astronomía, s/n, 18008, Granada, Spain
- ²⁰ Laboratoire d'astroparticules et cosmologie (APC), 10 Rue Alice Domon et Léonie Duquet, 75013 Paris, France
- ²¹ Instituto de Radioastronomía y Astrofísica (IRyA), Universidad Nacional Autónoma de México (UNAM), Antigua Carretera a Pátzcuaro # 8701, Ex-Hda. San José de la Huerta, 58341 Morelos, Mich., México
- ²² Instituto de Ciencias del Cosmos (ICC), Universitat de Barcelona (UB), Martí Franquès 1, 08028 Barcelona, Spain
- ²³ Universitat de Barcelona, Gran Via de les Corts Catalanes, 585, 08007 Barcelona
- ²⁴ European Space Astronomy Centre (ESAC), 28692 Villanueva de la Cañada, Madrid, Spain
- ²⁵ PITT PACC, Department of Physics and Astronomy, University of Pittsburgh, Pittsburgh, PA 15260, USA.
- ²⁶ Instituto de Física de Cantabria (Universidad de Cantabria - CSIC), Av. de los Castros, 39005 Santander, Cantabria, Spain
- ²⁷ Departamento de Física, Campus Reitor João David Ferreira Lima, s/n - Trindade, Florianópolis - SC, 88040-900, Brazil
- ²⁸ Finnish Centre for Astronomy with ESO (FINCA), University of Turku, Väisäläntie 20, 21500 Piikkiö, Finland
- ²⁹ Tuorla Observatory, Department of Physics and Astronomy, University of Turku, Väisäläntie 20, 21500 Piikkiö, Finland
- ³⁰ University of Warwick, Coventry CV4 7AL, UK
- ³¹ Institució Catalana de Recerca i Estudis Avançats (ICREA), Passeig Lluís Companys 23, 08010-Barcelona, Spain
- ³² Institute for Astronomy, University of Edinburgh, Royal Observatory, Blackford Hill, Edinburgh EH9 3HJ, United Kingdom
- ³³ European Southern Observatory, Karl-Schwarzschild-Str. 2, 85748 Garching, Germany
- ³⁴ Departament de Física, Universitat Politècnica de Catalunya, C/ Esteve Terrades 5, E-08860, Castelfelers, Spain
- ³⁵ Institute for Space Studies of Catalonia, c/Gran Capità 2–4, Edif. Nexus 201, 08034 Barcelona, Spain
- ³⁶ Instituto de Física (IF), Universidade Federal do Rio de Janeiro (UFRJ), C. P. 68528, CEP 21941-972, Rio de Janeiro, RJ, Brazil
- ³⁷ Department of Physics and Astronomy, University of Pennsylvania, 209 S 33rd St, Philadelphia, PA 19104, USA
- ³⁸ Universidad Complutense de Madrid, Departamento de Astrofísica, Facultad de Ciencias, Plaza de Ciencias, 1, Ciudad Universitaria, 28040, Madrid, Spain
- ³⁹ European Southern Observatory (ESO), Alonso de Córdova 3107, Vitacura, Santiago, Chile
- ⁴⁰ Campus Duque de Caxias, Universidade Federal do Rio de Janeiro (UFRJ), CEP 25245-390 Duque de Caxias, RJ, Brazil
- ¹ Centro de Estudios de Física del Cosmos de Aragón (CEFCA) - Unidad Asociada al CSIC, Plaza San Juan, 1, E-44001, Teruel, Spain
- ² Centro de Estudios de Física del Cosmos de Aragón (CEFCA), Plaza San Juan, 1, E-44001, Teruel, Spain
- ³ Instituto de Astrofísica de Canarias (IAC), Vía Láctea s/n. E-38205, La Laguna, Tenerife, Spain
- ⁴ Departamento de Astrofísica, Universidad de La Laguna (ULL). E-38206, La Laguna, Tenerife, Spain
- ⁵ Departamento de Astronomia, Universidade Federal do Rio Grande do Sul, Av. Bento Gonçalves, 9500 Porto Alegre 91501-970, RS, Brazil
- ⁶ Observatório Nacional do Rio de Janeiro (ON), Rua Gal. José Cristino 77, São Cristóvão 20921-400 Rio de Janeiro, RJ, Brazil
- ⁷ University of Michigan, Dept. Astronomy, 1085 S. University Ann Arbor, MI 48109, USA.
- ⁸ University of Alabama, Dept. of Phys. & Astronomy, Gallalee Hall, Tuscaloosa, AL 35401, USA
- ⁹ Observatório do Valongo (OV), Universidade Federal do Rio de Janeiro (UFRJ), Ladeira Pedro Antonio 43, 20080-090 Rio de Janeiro, Brazil
- ¹⁰ Instituto de Astronomia, Geofísica e Ciências Atmosféricas (IAG), Universidade de São Paulo (USP), Rua do Matão 1226, C. Universitária, São Paulo, 05508-090, Brazil